PPPL-2402

PPPL-2402

UC20-F

TOKAMAK PHYSICS STUDIES USING X-RAY DIAGNOSTIC METHODS

By

K.W. Hill, M. Bitter, S. von Goeler, P. Beiersdorfer, E. Fredrickson,
H. Hsuan, K. McGuire, N.R. Sauthoff, S. Sesnic, and J.E. Stevens

MARCH 1987

PLASMA
PHYSICS
LABORATORY

PRINCETON UNIVERSITY
PRINCETON, NEW JERSEY

PREPARED FOR THE U.S. DEPARTMENT OF ENERGY,
UNDER CONTRACT DE-AC02-76-CHO-3073.

TOKAMAK PHYSICS STUDIES USING X-RAY DIAGNOSTIC METHODS

K.W. HILL, M. BITTER, S. VON GOELER, P. BEIERSDORFER, E. FREDRICKSON, H. HSUAN, K. MCGUIRE, N.R. SAUTHOFF, S. SESNIC, and J.E. STEVENS

Princeton University
Plasma Physics Laboratory
Princeton, New Jersey 08544

PPPL--2402
DE87 010628

ABSTRACT

X-ray diagnostic measurements have been used in a number of experiments to improve our understanding of important tokamak physics issues. The impurity content in TFTR plasmas, its sources and control have been clarified through soft x-ray pulse-height analysis (PHA) measurements. The dependence of intrinsic impurity concentrations and Z_{eff} on electron density, plasma current, limiter material and conditioning, and neutral-beam power have shown that the limiter is an important source of metal impurities. Neoclassical-like impurity peaking following hydrogen pellet injection into Alcator C and a strong effect of impurities on sawtooth behavior were demonstrated by x-ray imaging (XIS) measurements. Rapid inward motion of impurities and continuation of $m=1$ activity following an internal disruption were demonstrated with XIS measurements on PLT using injected aluminum to enhance the signals. Ion temperatures up to 12 keV and a toroidal plasma rotation velocity up to 6×10^5 m/s have been measured by an x-ray crystal spectrometer (XCS) with up to 13 MW of 85-keV neutral-beam injection in TFTR. Precise wavelengths and relative intensities of x-ray lines in several helium-like

ions and neon-like ions of silver have been measured in TFTR and PLT by the XCS. The data help to identify the important excitation processes predicted in atomic physics. Wavelengths of n=3 to 2 silver lines of interest for x-ray lasers were measured, and precise instrument calibration techniques were developed. Electron thermal conductivity and sawtooth dynamics have been studied through XIS measurements on TFTR of heat-pulse propagation and compound sawteeth. A non-Maxwellian electron distribution function has been measured, and evidence of the Parail-Pogutse instability identified by hard x-ray PHA measurements on PLT during lower-hybrid current-drive experiments.

1.0 INTRODUCTION

X-ray diagnostics are used to measure a variety of plasma parameters of importance to tokamak physics and fusion research. In a companion paper /1/ the x-ray diagnostic instrumentation and data interpretation techniques are reviewed. This paper focuses on some significant experiments over the past few years in which x-ray diagnostic methods have played a key role in improving our understanding of tokamak phenomena. To represent the x-ray diagnostic capabilities as broadly as possible, work from PLT and Alcator C, as well as from TFTR, is presented.

In Section 2 a study of the variation of intrinsic impurities in the Tokamak Fusion Test Reactor (TFTR) /2/ with plasma parameters, machine conditioning, and different limiters is summarized; the soft x-ray pulse-height analysis system (PHA) was used for these measurements. The experiments suggest that the limiter, whether it be graphite or metal, is probably the dominant source of metal impurities in the plasma. The increase of metal concentrations with plasma current and with neutral-beam power and the decrease with electron density agree qualitatively with the notion of sputtering of the limiter by plasma and/or impurity ions. Section 3 reviews some observations on impurity transport and summarizes two recent studies of impurity transport that used the x-ray imaging system (XIS). First, following injection of hydrogen pellets into the Alcator C tokamak, the carbon and molybdenum density profiles were observed to peak in agreement with multi-ion neoclassical transport theory /3/. A large disruption reduced the central impurity density and terminated the neoclassical transport. The increase in central resistivity and the decrease following the disruption were accompanied, respectively, by an increase and then a decrease in sawtooth period. Second, experiments on the PLT tokamak used aluminum injection into

the plasma to study MHD behavior and impurity transport /4/. Inverted sawteeth on the central chord soft x-ray signals resulted from abrupt inward motion of the aluminum. Magnetohydrodynamic activity with m=1 structure was observed after the internal disruption. In Section 4 are presented some measurements by the x-ray crystal spectrometer (XCS) of the ion temperature and plasma toroidal rotation velocity in TFTR during intense neutral-beam heating experiments. Central ion temperatures greater than 12 keV and toroidal rotation velocities up to 6×10^5 m/s were measured for deuterium neutral-beam injection powers up to 13 MW. Section 5 summarizes some results of a study of the Kα resonance line and satellites of helium-like titanium using the XCS on TFTR /5/. The intensities of most lithium-like and beryllium-like satellites, relative to the helium-like titanium resonance line, agree well with predictions. The intercombination and forbidden lines are more intense than predicted for electron temperatures below 1 keV. A review of some of the findings in an XCS study of neon-like silver spectra on PLT is presented in Section 6 /6/. Wavelengths of pairs of n=3 to 2 electric dipole and electric quadrupole lines were measured precisely, yielding accurate wavelengths for $\Delta n = 0$ transitions of interest in x-ray laser studies. The Kα lines of hydrogen-like and helium-like ions of several elements provided excellent reference wavelengths. In Section 7 measurements using an XCS of neutral hydrogen density in Alcator C are summarized /7/. The neutral hydrogen density is inferred from the enhancement of $1s^2 - 1snp$ lines in Ar^{+16} for $3 \leq n < \infty$ due to charge transfer from neutral hydrogen to Ar^{+17}. Section 8 summarizes recent theoretical and experimental (XIS) work on measurement of the electron thermal diffusivity in TFTR from heat-pulse propagation /8/. In Section 9 XIS studies of compound sawteeth in TFTR are reviewed briefly /9/. Finally, in Section 10 some results are presented from

a study of the electron distribution function during lower-hybrid current-drive (LHCD) experiments on PLT /10-12/. Observation of a relaxation oscillation consistent with the Parail-Pogutse instability is presented /13/.

2.0 INTRINSIC IMPURITY BEHAVIOR IN TFTR

Impurities play an important role in determining plasma characteristics in tokamaks. The concentration of impurities is determined not only by the impurity sources but by transport. The main deleterious effects of impurities are dilution of fusion fuel, loss of energy by radiation, creation of instabilities through modification of the current profile /14/, and, perhaps, enhanced erosion of the limiter due to the higher sputtering yield by typical impurity ions than by deuterium /15,16/. Impurity control will be crucial at reactor power levels, since impurity production appears to increase with input power. The soft x-ray PHA diagnostic has been used to study the behavior of intrinsic metal and low-Z impurities and Z_{eff} in TFTR /2/ as a function of electron density, plasma current, plasma size, internal vacuum vessel hardware and its proximity to the plasma, machine conditioning, and neutral-beam injection power. The studies have improved our knowledge of impurity sources, particularly of the metals, and of impurity control techniques. A summary of some of the main results and conclusions of the TFTR study will be given here.

The behavior of metal concentrations in TFTR suggests that sputtering of the limiter by plasma and/or impurity ions may be the dominant source of metal impurities. The central plasma concentration of typical metals (titanium, chromium, iron, and nickel) was observed to decrease with line-averaged electron density $\bar{n}_e$ and to increase with plasma current I_p as shown in Fig. 1. These plasmas had a major radius R of 2.45 - 2.55 m, a minor radius a of 0.82 m, and either a graphite limiter or a titanium-carbide-coated graphite

limiter. This type of behavior has been observed on other tokamaks, but the TFTR study quantified the observations for a variety of machine parameters. Three interesting points to notice are that (1) the decrease with n_e is approximately exponential, perhaps with two different slopes in some cases, (2) the magnitude of the slope decreases as plasma current increases, and (3) the magnitude of the slope is smaller for smaller plasma radius (not shown in Fig. 1). A similar effect is observed for the total low-Z impurity concentration, although the decrease with density is much less pronounced and varies considerably less with plasma current and size. These trends are consistent with a picture in which the impurity source, particularly for the metals, is due to sputtering of the limiter (and/or other hardware) by plasma and/or impurity ions. The average energy of an ion striking the limiter should be proportional to the sheath potential and, thus, proportional to the electron temperature /16,17/. Lower edge temperatures and, thus, decreased sputtering should occur for either (1) higher density, (2) lower current, or (3) larger plasma size. This picture is, however, qualitative. A discussion of the more complicated aspects of impurity production, shielding from the plasma center, and confinement is beyond the scope of this paper. Also, other impurity source mechanisms may come into play /17/.

Other experiments during the earlier periods of operation of TFTR further implicated the limiter as the dominant source of metal impurities in the plasma. First, the titanium concentration was 50 times higher with a titanium-carbide (TiC)-coated graphite limiter than with an uncoated graphite limiter /2,18/. Second, the nickel concentration was 20 times higher when the plasma was operated on the Inconel bellows cover plates than on a TiC-coated graphite moveable limiter. Third, for plasmas operated on a graphite or a TiC-coated graphite limiter (See Fig. 2) the plasma central nickel

concentration at fixed density was observed to decrease gradually with plasma operation after pulse-discharge cleaning (PDC). Since metals are generally higher after PDC, it is believed that the PDC and preceding glow-discharge cleaning (GDC) remove metal from the vacuum vessel wall and other metal hardware inside the vacuum vessel and deposit some of it on the limiters. The concentrations in Fig. 2 decrease with the number of plasma shots, N, after pulse-discharge cleaning according to $N^{-0.6}$.

The low-Z impurity concentrations and Z_{eff} are also inferred from the PHA x-ray spectrum. The low-Z concentrations are obtained by taking the measured continuum intensity and subtracting a portion due to recombination and bremsstrahlung of electrons with the metals whose concentrations are known from line radiation /2,19-21/. The remaining continuum intensity is compared with the bremstrahlung intensity expected for a pure hydrogen or deuterium plasma. The enhancement of this intensity above that for a pure plasma is attributed to electron bremsstrahlung and recombination with low-Z impurities. Since the dominant low-Z impurity in TFTR has been identified by vacuum ultraviolet (VUV) spectroscopy as carbon /22/, except at very high density where oxygen becomes comparable, it is then easy to calculate how much fully stripped carbon is required to produce the measured continuum enhancement. The proton or deuteron density is then calculated from the charge neutrality requirement, and the plasma resistivity or Z_{eff} follows from a knowledge of the density of all ion species. The total low-Z concentrations inferred from the PHA typically range from 10% of electron density at the lowest densities to < 1% at high densities. These concentrations have a larger uncertainty than do the metal concentrations, since the continuum-enhancement factor is difficult to measure.

Some measurements of Z_{eff} in TFTR by the PHA are illustrated in Fig. 3 for ohmically heated deuterium plasmas with a current of 2.2 MA. These data show that Z_{eff} for operation on the outer moveable limiter blades or on the inner toroidal bumper limiter, approaches values ≤ 1.5 at high density. At intermediate densities bumper-limiter operation shows somewhat lower Z_{eff} /23/. For this comparison, model profile shapes for temperature and density were used in the analysis from both data sets. Reanalysis of the bumper-limiter data using measured Thomson scattering profiles for these parameters has given Z_{eff} values 0.2-0.4 higher than the values shown in Fig. 3.

The source of the low-Z impurities is harder to determine from PHA data since the PHA cannot distinguish between carbon and oxygen. Vacuum ultraviolet spectroscopic studies show that the carbon concentration decreases with $\bar{n}_e$ in ohmic discharges. A comparison of these data with sputtering yields suggests that the carbon impurity could be explained by self-sputtering of the graphite limiter /15/. The oxygen concentration, however, is observed to increase with density /22, so its production mechanism is probably different from that of carbon.

Intrinsic impurity concentrations are higher in neutral-beam-heated discharges than in ohmic-heated (OH) discharges with the same electron density, current, toroidal field, and radius /24/. This is not unexpected since the electron /25/ and ion temperatures and the power to the limiter increase with beam heating. The enhancement of impurities relative to the ohmic values is graphed versus total power in Fig. 4 for plasmas on the graphite moveable limiter. The metals have a stronger dependence on beam power than do the low-Z impurities. It is also true that the dependence of metal concentrations on current and density are in general much stronger than for low-Z concentrations.

The points in Fig. 4 were obtained by dividing the concentration of an impurity obtained during neutral-beam heating by the impurity concentration just before the beams were turned on and multiplying by a factor to correct for the increase in electron density due to beam fueling. This correction factor is taken from a curve such as that shown in Fig. 1, so that we can, in the same shot, compare the impurity concentration during beam heating with that of an ohmic-heating value extrapolated to the same density as that for beam heating. This procedure has been adopted since the metal layer on the limiter can vary with conditioning, and reference ohmic-heating density scans are made very infrequently.

The enhancements shown in Fig. 4 appear to be largely an artifact of the experimental procedure. To ensure that all plasmas had the same density near the end of the beam-fueling phase, it was necessary to decrease the pre-beam density with increasing beam power. Hence, shots with higher beam powers had higher pre-beam impurity concentrations. Since impurity densities have been observed to change little from the pre-beam to the beam-heated phase of a shot, the impurity content during beams reflects mainly the content before beams. Thus, while impurity sources may increase due to increased edge temperatures with neutral-beam heating, this effect cannot be isolated from the data of Fig. 4 because of the large variations in pre-beam impurity content.

3.0 IMPURITY TRANSPORT

Neoclassical transport theory predicts an accumulation of impurities in the center of tokamaks or a peaking on axis /3,14,26/. Impurity accumulation has been observed in recent years in several tokamaks in regimes of interest for fusion /3,14,27,28/. Such behavior can adversely affect the current

profile and, therefore, the stability of plasmas. Also, as the heating power increases in tokamaks, in general, the production of impurities appears to increase. The combination of increasing source strength of impurities and accumulation or peaking in the center could have severe consequences for future reactors.

The study of impurity transport has received renewed interest in recent years. Instabilities such as the sawtooth have been shown to have a strong effect on impurity transport /29,30/. Conversely, impurity peaking has been shown to affect the sawtooth and possibly to enhance the m=1 instability, and to cause or increase the frequency of major current disruptions at high density /14/. In many of the impurity transport experiments x-ray diagnostics, and particularly the XIS, have been primary measurement tools because of their good spatial and temporal resolution, and their capability to respond preferentially to impurity radiation. The goal of these experiments, as usual, has been to obtain a better basic understanding of the physics processes underlying the transport. An improved understanding of these phenomena should, hopefully, guide experimenters to regimes in which the deleterious impurity effects are subdued, in order to permit plasma conditions more favorable for fusion. In this section, an overview of two recent studies of impurity transport is presented. Experiments on impurity accumulation and on the redistribution of impurities due to internal disruptions are emphasized. X-ray diagnostics played a major role in these experiments.

3.1 IMPURITY PEAKING WITH PELLET INJECTION

During hydrogen pellet injection experiments in Alcator C, two phenomena have been observed by means of XIS measurements /3/. First, following the pellet injection a central accumulation or peaking of carbon (C) and

molybdenum (Mo) was observed, in agreement with multi-ion neoclassical impurity diffusion theory. Second, direct evidence was observed that the impurity transport affects the sawtooth dynamics.

The spatial evolution of the impurities was measured with two XIS arrays having different filters. A thin foil allowed one array to respond strongly to the Mo L x-ray lines near 2.5 keV. A second XIS array had a foil thick enough to block the Mo radiation, and thus it responded strongly to the carbon bremsstrahlung and recombination radiation, as well as to the hydrogen bremsstrahlung. In order to infer impurity concentration profiles, Abel-inverted emission profiles were compared to theoretical emission calculations that used measured electron temperature and density profiles and the XIS response functions.

Signals from several chords of the XIS array that was sensitive to Mo radiation are shown in Fig. 5a and b. The chords are 1.7 cm apart. The top signal is from the central chord. At t = 223 ms the pellet enters, and the electron temperature drops from 1.6 to 0.6 keV. During the reheat phase the impurity profiles become peaked, and the sawtooth period lengthens; in many cases the sawteeth disappear. The impurity peaking agrees with a multi-ion neoclassical transport model (see Fig. 6). Following the large disruption near 259 ms the central impurities drop by a factor of 3, the neoclassical-like transport terminates, and the sawtooth period shortens by a factor of 2.5 approximately 15 ms later. Figure 5c shows the x-ray emissivity profiles just before the pellet, and enters just before (257.5 ms) and just after (259.3) the large disruption.

Radial profiles of (a) carbon density, (b) Mo density, (c) electron density, (d) electron temperature, (e) hydrogen density, and (f) Spitzer conductivity, are shown in Fig. 6 just before (i) and after (ii) the large

disruption. The dashed curves are the neoclassical equilibrium predictions, which agree quantitatively with measurements for carbon, but are just outside the error bars for Mo.

For cases in which the sawteeth disappear after the pellet enters, large disruptions do not occur and the highly peaked impurity profiles persist. For cases with sawteeth, the carbon profile does not dramatically repeak after the large disruption. The increasing sawtooth period during impurity peaking and the decreasing period after the impurity profile flattens suggest that the sawtooth dynamics are affected by the changes in the conductivity profile (Fig. 6f).

3.2 IMPURITY TRANSPORT AND MHD ACTIVITY WITH ALUMINUM INJECTION

A recently published experiment with laser-injected aluminum in PLT discharges illustrates the use of the XIS to study both MHD behavior and impurity transport /4/. Aluminum injection into PLT discharges with normal sawtooth oscillations made it possible to observe the persistence of m=1 activity on x-ray traces after an internal disruption. The m=1 activity is normally not observable after an internal disruption in nonimpurity-injected plasmas. Furthermore, numerical simulations of the impurity transport and the chordally integrated x-ray emission were able to explain the unusual suppression or inversion of the normal sawtooth drop on the central soft x-ray (SX) and ultrasoft x-ray (USX) traces in plasmas following the aluminum injection.

The inverted sawteeth on the central x-ray trace is illustrated in Fig. 7. It is preceeded by a sharp rise and saturation of the intensity. A similar time behavior is observed on the central USX trace, although usually two inverted sawteeth are observed. The internal disruption associated with

the inverted sawtooth is labeled the principal internal disruption. Simulations show that the sharp rise in intensity after aluminum injection is due to hydrogen-like and helium-like aluminum lines and recombination radiation. The Kα lines of these species are at 1.73 and 1.59 keV, respectively. The 1/e cut-off energy of the 76-micron-thick SX beryllium filter is 2 keV, and for the 13-micron-thick USX beryllium filter it is 1.1 keV.

Both the inverted sawteeth and the subsequent persistence of m=1 activity after the internal disruption on the SX and USX traces are shown in Fig. 8. This figure also illustrates more clearly the main features on the central SX (top traces), USX (middle traces), and electron temperature (bottom curves) before, during, and after the time of impurity injection and principal internal disruption. The T_e measurements were made from the second harmonic of the electron cyclotron emission. The x-ray traces (left curves) evolved from the normal sawtooth before impurity injection to a sharp rise after impurity injection, a saturation, either one or two inverted sawteeth, and subsequent normal sawteeth. The normal sawteeth on the T_e trace appear to be unchanged by the aluminum injection. This suggests that the impurity injection does not alter the MHD activity. The central and right-hand set of curves show expanded views of the three signals before (center) and after (right) aluminum injection. The m=1 oscillations are present before a sawtooth drop and absent after a sawtooth drop on all three signals before aluminum injection. The sawtooth-like behavior of the SX and USX traces is, of course, due to modulation of the plasma bremsstrahlung and intrinsic impurity radiation by the sawteeth variations in T_e. After aluminum injection, however, the m=1 activity disappears (as usual) on the T_e trace but continues essentially unchanged in amplitude on the SX and USX traces, although the period is slightly larger.

The interpretation of the inverted sawteeth is as follows: initially the radial profile of the injected aluminum impurity density is hollow. The principal internal disruption tends to abruptly fill the center with aluminum. The increase in emission from the higher aluminum density can be equal to or larger than the decrease in emission of each ion due to the sudden drop in T_e. Similar hollow profiles of silicon in the helium- and hydrogen-like charge states were observed in Alcator C /29/. Following an internal disruption the radial profiles are flattened through an abrupt inward motion of silicon.

The fast disappearance of the m=1 signature on the central T_e signal during both normal sawteeth and the sawteeth at the inverted disruption results from a flattening of the T_e profile. This flattening also accounts for the disappearance of the m=1 signature on the x-ray traces. The presence of the post-disruptive SX and USX m=1 oscillations with impurity injection is interpreted as being due to either (a) an excess of aluminum in the m=1 magnetic island compared to the central core of the plasma, or (b) a lack of penetration of aluminum into the island, leaving an eccentric radiating inner core. In case (b) the island itself is weakly emitting. Further studies are required to identify which of these hypotheses is correct.

4.0 ION TEMPERATURE AND TOROIDAL ROTATION VELOCITY

The x-ray crystal spectrometer in recent years has become a well established diagnostic for measuring the ion temperature in tokamaks /5,31-34/. It is especially useful for measuring temperature in the hot central core of large, dense, neutral-beam-heated tokamaks where other ion temperature diagnostics experience difficulties /31/. It is also useful for measuring toroidal rotation velocity in tokamaks /5,35,36/. The ion temperature is

measured from Doppler broadening of x-ray lines of typical helium-like or hydrogen-like medium-Z ions such as Ar, Ti, Cr, Fe and Ni. In order to measure toroidal rotation velocity the spectrometers on TFTR are oriented such that their line of sight has a tangential or toroidal component. Thus, motion of the ions toward or away from the spectrometer due to toroidal plasma rotation imparts a Doppler shift to the x-ray lines, which can be used to measure the rotation velocity and direction. Descriptions of the instruments have been given elsewhere /1,31-33,37,38/. In this section, results of measurements from TFTR are presented.

Figure 9 illustrates both the measurements of ion temperature and toroidal rotation in TFTR. The curves at the left are measured spectra of the titanium XXI resonance line at 2.61 Å integrated over the indicated consecutive 60-ms time intervals. The solid lines are a least squares fit to the data using a Voigt function, which accounts not only for Doppler broadening but also for the spectrometer resolution and the natural line width. The lines are perceptibly broadened, and the centroid is shifted toward higher channel number or longer wavelength. The values of ion temperature inferred from the broadening are shown on each spectrum and are graphed versus time in the top right curve. The shift toward longer wavelength indicates plasma motion away from the spectrometer. The rotation velocity and direction can be calculated from the Doppler shift, since the spectrometer line of sight points toward the counter-clockwise direction at an angle of 22 degrees relative to the plasma center line. The curves on the right show the time evolution of the ion temperature and counter-clockwise toroidal rotation velocity v_t from 2.0 to 3.5 s during a discharge which has 3.6 MW of 85-keV deuterium beams injected from 2.5 to 3.0 s. The other plasma parameters were I_p = 0.7 MA, B_T = 3.9 T, R = 2.56 m, and minor radius a = 0.82

m. During neutral-beam injection (NBI) the temperature of the titanium XXI ions increases from 2 keV to a peak value of 13 keV. Also, the plasma spins up to a rotation velocity of just under 6×10^5 m/s, which is greater than the average ion thermal velocity.

The saturation and drop in ion temperature before the end of the beam pulse probably results from beam fueling. During neutral-beam injection the line-averaged electron density $\bar{n}_e$ rises continuously from 4.5×10^{12} to $8.5 \times 10^{12} cm^{-3}$. This increase in cold electrons tends to cool the ions, especially since the electron-ion coupling increases at the higher density. The peak electron temperature at t = 2.9 s was 3.8 keV, and the peak density was $2 \times 10^{13} cm^{-3}$.

After the NBI is terminated at 3.0 s both T_i and v_t show a delay in returning to their values before NBI. Immediately after t = 3.0 s there still exist fast beam ions since the slowing down time is 100 ms. These ions continue to impart angular momentum to the plasma and continue heating it until they have thermalized. After this first 100 ms, the decay in v_t can be related to a momentum confinement time, which is typically 200-300 ms. More details of the rotation measurements and modeling are presented in Ref. 36.

5.0 HELIUM-LIKE TITANIUM Kα SPECTRA

High-resolution x-ray crystal spectrometers (XCS) on tokamaks have provided a unique opportunity to study experimentally inner-shell excitation and dielectronic recombination processes in 1, 2, and 3 electron medium-Z impurity ions (Z = 18 - 28). For these relatively simple ions, atomic physics computer codes have some hope of making reliable predictions. The excellent energy resolution ($E/\Delta E \sim 10^4$) and dispersion of the XCS permits recording of very high quality spectra and very precise determination of wavelengths. The

tokamak x-ray source has relatively low density (n_e = 10^{13} - $10^{15}cm^{-3}$), and thus is relatively collisionless. This means that (1) the impurity ions are predominantly in the ground state, and (2) once excited, e.g. from the n=1 to n=2 level, the electron impact collisional excitation and de-excitation rates are usually small compared to radiative or Auger decay rates or recombination. Furthermore, the line broadening for ion temperatures of 1 to 2 keV is dominated by Doppler effects, which are small compared to broadening in high density plasmas such as those produced by lasers, and the relatively long time scales allow a steady-state ionization balance to be achieved.

The spectra of helium-like impurity ions have received a lot of attention, both experimental and theoretical /5,33,39,40/, since the two-electron ion is relatively simple and exists in tokamaks over a wide range of electron temperatures. Also, for these reasons, these spectra are ideal for diagnostics of both laboratory and astrophysical plasmas. In general, the theoretical predictions have done quite well in predicting observed spectral features. In this section, some of the results of a study of helium-like titanium in TFTR are presented.

Kα x-ray spectra of helium-like titanium and satellites, measured by the XCS on TFTR, have been compared with recent theoretical predictions /5/. Agreement is generally good, although some deficiencies in the theory remain. Figure 10a shows that the data points agree well with a synthetic spectrum (solid curve) calculated from atomic data with some adjustments. The various contributions to the synthetic spectrum are shown in Fig. 10b, c, and d. In Fig. 10b we see that the theoretical intensities for the intercombination (x,y) and forbidden (z) lines, as shown by the darkly shaded peaks, underestimate the measured intensities. Here the dotted regions were obtained from least squares fits of Voigt functions to the data. Figure 10c

shows lithium-like satellites due to transitions of the type $1s^2nl$ - 1s2pnl with $n > 2$. Figure 10d shows both Li-like lines produced by collisional inner-shell excitation and Be-like satellites excited by dielectronic recombination of Li-like ions. An adjustable parameter used in the fit was the ratio of the abundance of Li-like to He-like charge states.

The theoretical underestimates of lines x, y, and z are illustrated in Fig. 11 as a function of electron temperature. The theoretical lines were calculated for direct electron impact excitation from the ground state (solid line) and excitation to levels $n \geq 2$ including cascading (dashed lines). Agreement between theory and experiment (points) generally improves at higher temperature. Cascade corrections worsen agreement for line x but generally improve agreement for lines y and z. Interestingly, predictions for the sum of intensities of the three lines $(I_x + I_y + I_z)/I_w$ agree well with measurements for $1.2 < T_e < 2$ keV, but are too low by a factor of 8 for T_e = 0.6 keV. The experimental enhancement of intensity appears to be related to the increase in the Li-like charge state at low temperatures.

6.0 NEON-LIKE SILVER

Recently, high resolution n = 3 to 2 (where n is the principal quantum number) x-ray spectra of neon-like silver in the wavelength range 3.36-4.1 Å have been measured with an x-ray crystal spectrometer (XCS) on the PLT tokamak /6/. These studies have provided new insights into precise wavelength calibration techniques and the accuracy of wavelength measurements for x-ray crystal spectrometers, as well as an experimental verification of wavelengths calculated by atomic physics codes. This information is important both for plasma diagnostics and for basic atomic physics. The measurements have also provided an improved knowledge of intra-shell energy separations of levels

which are important candidates for x-ray lasers and of transition rates in neon-like as well as sodium-, magnesium-, and aluminum-like ions of silver.

The spectra of medium- and high-Z neon-like ions are useful for diagnostic purposes because they are prominent over a wide range of plasma parameters in tokamaks and other plasma sources. This fact is due to the closed-shell configuration and the resultant stability of the ions. Furthermore, accurate measurements of wavelengths of transitions in such multi-electron ions are important, especially for high-Z, because configuration interaction and quantum electrodynamic effects can reduce the accuracy of wavelength calculations. An advantage of using high-Z ions for these neon-like 3-2 transitions is that electric quadrupole (E2) transitions become comparable to electric dipole (E1) transitions. This results in pairs of E1 and E2 quadrupole lines whose energy separations are equal to the transition energies in $\Delta n = 0$ transitions of importance for population inversions.

Tokamak plasmas are particularly useful for studying transitions in high-Z ions because the electron densities are low enough to render collisional depopulation of excited states, such as the $n = 3$ states of neon-like silver, negligible. Also, the long time scales relative to, e.g., laser-produced plasmas allow a steady ionization balance to be achieved in tokamaks. The PLT study extended the observation of neon-like states in tokamaks from the highest Z (42) previously observed to the present record of Z=47. Neon-like ions of even higher atomic number should be attainable in TFTR, which has recently reached electron temperatures greater than 6 keV.

Figure 12 illustrates the lines of interest for this experiment. This is a Grotrian diagram of the ground state and selected first excited states of the neon-like ion. The important transitions for the x-ray laser experiments

are indicated by the dashed lines connecting the left $2p^5 3s$ levels to the central $2p^5 3p$ levels. A low decay rate to the ground state for the electric quadrupole transitions labeled E2 relative to the electron dipole transitions labeled 3G and 3F permits a population inversion between the $2p^5 3s$ and $2p^5 3p$ levels to occur. The laser transitions, however, are difficult to identify by UV or soft x-ray spectroscopy in plasmas because they occur in regions dominated by stronger $\Delta n = 0$ transitions in ions of neighboring charge states. Hence, simultaneous measurements of the wavelengths of E1 transitions 3G and 3F and the E2 transitions can provide an accurate measure of the wavelengths of the lasing transitions.

The silver was introduced into the tokamak by the laser injection technique. Figure 13 shows a portion of the spectrum measured on PLT, which illustrates the line 3G and the corresponding E2 transition. This spectrum has been simplified by subtraction of a spectrum taken without silver injection into the plasma in order to remove strong lines of intrinsic impurities. The energy interval between these lines is 124.1 eV. The theoretical interval is 123.5, calculated by a relativistic atomic structure code. The center position of a line is obtained from a least squares fit of a Voigt function to the data. The uncertainty in the center position of these lines is approximately ±0.1 mÅ.

For precise wavelength measurements an accurate calibration of the XCS is required. For this experiment $K\alpha$ resonance lines of several hydrogen and helium-like ions were used for reference wavelengths. The reference spectra are similar to the He-like Ti spectra of Fig. 10. The positions of these reference spectral bands on the first-order silver spectrum are illustrated by the shaded regions in Fig. 14. The shorter wavelength Fe and Mn lines were measured in second order; thus, the wavelength scale in Fig. 14 should be

divided by 2 for these ions. The resonance lines of these 1 and 2 electron ions are well suited as wavelength references because they can be calculated theoretically to a high degree of accuracy. The large number of strong reference lines covering the spectral region of interest served two purposes. First, they provided a nearby, strong H- or He-like reference line for each of the lines to be measured. The estimated uncertainty in the silver lines due to uncertainties in the dispersion of the spectrometer were thus reduced to less than 0.15 mÅ. Second, they allowed a very precise comparison of nearby lines of both H- and He-like ions. In general, close agreement was found between the measured and theoretical wavelengths for these many reference lines. However, a discrepancy of 0.4 mÅ was observed between theory and experiment for the H-like line of argon when the He-like iron line w was used as a reference. This is larger than the experimental uncertainty in the measurements and suggests that theoretical calculations for these systems should be revised.

In summary, high resolution measurements of a range of x-ray lines from neon-like silver in the region 3.36-4.1 Å have been made. The wavelengths of both electric dipole and electron quadrupole lines in the n=3-2 spectra have been measured very precisely, thus establishing experimental energy intervals for transitions of interest in x-ray laser research. Several strong calibration lines of helium-like and hydrogen-like ions have provided very accurate references, thus demonstrating a very precise calibration scheme for the XCS. Some discrepancies in theoretical calculations of Kα transitions for these systems have been observed. In addition, many lines of sodium-, magnesium-, and aluminum-like silver have been identified. Also, intensity calculations have been made for many of the features and have been compared with the spectra. An improved understanding of neon-like systems should

increase their suitability for plasma diagnostics, similar to the applications of helium-like and hydrogen-like ions.

7.0 NEUTRAL HYDROGEN DENSITY MEASUREMENTS

Recent XCS measurements of helium-like argon x-ray spectra have enabled measurement of the neutral hydrogen (H_o) density profile ($n_o[r]$) in the Alcator-C tokamak /7/. The H_o density was inferred from the enhancement of lines from the transition $1snp \rightarrow 1s^2$ with $3 \leq n \leq \infty$ due to charge transfer between intrinsic H_o and hydrogen-like argon (Ar^{+17}). Charge transfer to Ar^{+17} from H_o in its first few excited states was also observed for the first time.

Spectra which illustrate the charge-transfer process are shown in Fig. 15. These are the $1snp \rightarrow 1s^2$ transitions in Ar^{+16} measured from different chords of Alcator C following the introduction of Ar into the discharge. The quantum number n is indicated near the peaks. The parameter h represents the perpendicular distance of the viewing chord from the center of the plasma. The limiter radius was 16.5 cm. The intensities of the lines for $n = 9$ and 10 are strongly enhanced relative to the lines $n = 8$ and 11 for outer radii. This enhancement is consistent with the charge-transfer process since the process is predicted to have a strong dependence on the n level of the recombining ion with a maximum near $n = 9$. The enhancement is expected to be larger at outer radii because there is a relatively large neutral density and electron impact excitation of the np levels is negligible because of the low electron temperature (≤ 300 eV). Measurements extending to shorter wavelengths show an intense, broad feature at the location corresponding to $n = 27$ with a shoulder near the wavelength for $n = 18$. These observations are interpreted as charge transfer from hydrogen atoms in the first two excited

levels to Ar^{+17} since, again, these are the quantum numbers predicted for the maximum of this process.

In order to interpret the measurements, the Abel-inverted emission profiles were compared with a model for the line intensities which included the processes of electron impact excitation of Ar^{+16} from the ground state, radiative recombination of ground state Ar^{+17}, and radiative decay of the excited np levels. The density profiles for ground state Ar^{+16} and Ar^{+17} were obtained from an impurity transport simulation. Calculated emission profiles for the various lines in Fig. 15 were in excellent qualitative agreement with measurements for $r \leq 9$ cm.

The enhancements outside $r = 9$ cm of the measured emission profiles relative to the calculations for $n = 9$ and 10 were used, along with available charge-transfer cross sections, to determine the hydrogen neutral density profile. The results are illustrated in Fig. 16. The data points inferred from the broad spectral feature for $n \geq 15$ (the excited-state hydrogen) required further assumptions and have been normalized to the $n = 9$, 10 data at $r = 12$ cm. The results are in good agreement with simulations from the FRANTIC neutral transport code.

Further information obtained was an order-of-magnitude estimate of the cross section for charge transfer to Ar^{+17} from the excited levels of H_o. This was deduced from the measured neutral density profile and the enhanced spectral feature for $n > 15$. The results are $\langle \sigma_{n=2} v \rangle / v_{th} \approx 10^{-13}$ cm^2 and $\langle \sigma_{n=3} v \rangle / v_{th} \approx 2.5 \times 10^{-13}$ cm^2, where $\langle \sigma v \rangle$ is a rate coefficient averaged over a Maxwellian neutral thermal distribution.

The uncertainty in the absolute value of n_o in Fig. 16 is estimated to be about a factor of 5. The n_o profile shape, however, should be much less uncertain, as indicated by the error bars.

8.0 HEAT-PULSE PROPAGATION STUDIES

Electron heat diffusivity χ_e is another parameter which can be measured by x-ray imaging (XIS)/8/. A knowledge of this quantity is important since anomalous heat conductivity is generally thought to dominate the energy loss mechanisms in large tokamaks such as TFTR. Few direct methods have been available to measure this quantity locally. However, the χ_e measured by the XIS on TFTR usually exceeds that determined from power balance considerations by a factor ranging from 2 to 10 (Fig. 17). This discrepancy is presently not understood, and resolution could elucidate the anomalous transport mechanisms present in large tokamaks such as TFTR.

The technique of measuring χ_e in tokamaks using the XIS involves measuring the radial propagation of heat pulses produced by naturally occurring sawtooth oscillations. This technique was first used on ORMAK /41/. A brief historical survey of this type of measurement is given in Ref. 8. Recently, extensions of this work were done on TFTR for two reasons: (1) the time scales for sawtooth repetition and propagation of heat pulses to the edge of the plasma are much longer (tens of milliseconds) in large tokamaks than in smaller ones; (2) excellent x-ray imaging data and fast (few ms) electron temperature profile data from electron cyclotron emission were available /42/.

The recent work on heat-pulse propagation was based on a solution of the electron heat balance equation following a small, sawtooth-induced electron temperature perturbation $\tilde{T}(r,t)$ from an equilibrium profile. The spatial and temporal evolution of the perturbation evolves according to the equation

$$\frac{3}{2} n_e \frac{\partial \tilde{T}(r,t)}{\partial t} = \frac{1}{r} \frac{\partial}{\partial r} \left[r n_e \chi_e \frac{\partial \tilde{T}(r,t)}{\partial r} \right] . \qquad (1)$$

A solution derived by Soler and Callen /43/ is

$$\tilde{T}(r,t) = \frac{A^2 r_1 r_s \tilde{T}_o}{2t} e^{-A^2 r^2/4t} \left[e^{-A^2 r_2^2/4t} I_o\left(\frac{A^2 r r_2}{2t}\right) - e^{-A^2 r_1^2/4t} I_o\left(\frac{A^2 r r_1}{2t}\right) \right] \tag{2}$$

Here t is the time measured from the sawtooth crash at time t_o, $A^2 = 3/2\chi_e$, r_s is the q = 1 or inversion radius (related to the reconnection radius r_o by $r_o \leq 2\, r_s$, and I_o is a modified Bessel function. The initial temperature perturbation was a negative and a positive delta function of magnitude $\tilde{T}_o$ at positions r_1 and r_2, respectively, where $0 < r_1 < r_s$ and $r_s < r_2 < r_o$. Other assumptions required to derive Eq. (2) were that n_e and χ_e are constant with radius.

The study of heat-pulse propagation in TFTR involved comparison of both x-ray emissivity and electron temperature profile evolution with solutions of Eq. (1), both the analytic solution, Eq. (2), and numerical solutions. The comparisons have indicated that the sawtooth-generated heat pulses are diffusive in nature, i.e., their behavior can be described by Eq. (1). Furthermore, it was shown that the solutions of Eq. (1) were insensitive to most of the assumptions used in deriving Eq. (2), i.e., initial pulse shape and electron density profile. The values of χ_e derived from this analysis, however, are consistently larger by a factor of 2-10 than the χ_e derived from the plasma global power balance as illustrated in Fig. 17. This discrepancy is still unresolved, although some possible explanations have been suggested.

A number of techniques were used to compare TFTR data with the solution Eq. (2) of the diffusive heat-pulse propagation model and, thus, to confirm the diffusive nature of the observed heat pulses. The first involves the time-to-peak of pulses at various radii. A large Bessel function argument

expansion of Eq. (2) and differentiation to find the time-to-peak t_p led to the result

$$\Delta t_p = \frac{\Delta r^2}{9\chi_e} \quad . \tag{3}$$

This suggests that a plot of the time-to-peak as a function of radius squared should be linear with slope 1/9 χ_e. Figure 18 shows such a plot for TFTR XIS data, supporting the diffusive nature of the pulses and providing a measure of χ_e. Figure 18 also shows that the heat pulse which is sometimes seen resulting from the first sawtooth crash (the "event") is much slower than pulses propagating from normal periodic sawteeth.

A second method of data reduction involves the pulse shape or time evolution of the heat pulse at a fixed radius. An expression derived from Eq. (2) for this pulse shape is graphed as the points and smooth curve in Fig. 19. This pulse shape agrees well with the rough curve, which is the T_e perturbation measured from electron cyclotron emission by a radiometer /42/. This agreement further verifies the diffusive nature of the heat pulses. The electron thermal diffusivity χ_e can be derived by either doing a least squares fit of the analytical pulse shape to the data or by finding the decay time from peak to half maximum. A further check on the diffusive nature of the measured heat pulses is the radial dependence of the maximum of the temperature perturbation, which is observed to decrease approximately as r^{-4}, in agreement with the analytic solution of Eq. (1).

A third technique of reducing the heat-pulse propagation data, which is less sensitive to inaccuracies due to pileup of multiple pulses or to the specific model assumed for the initial temperature perturbation, is the phase shift analysis. This technique has been used to find radial profiles of $\chi_e(r)$, rather than a cylindrically averaged χ_e.

In order to check the analytic solution Eq. (2) and to verify that it has no gross model dependencies, Eq. (1) was solved numerically for various conditions. It was verified that different initial temperature perturbations, opposing positive and negative delta functions, square waves, or parabolas resulted in only minor variations in the t_p versus r^2 curves. Also, realistic electron density profiles resulted in approximately the same solution as the constant $n_e(r)$ assumed in deriving Eq. (2). Multiple-pulse effects were shown to increase the inferred χ_e by at most a factor of 2. However, if the time for propagation of the heat pulse is less than one fourth the sawtooth period, the effect of multiple pulse pileup on χ_e is less than 15%.

The assumption having the largest effect on the calculated t_p versus r^2 curves is that of nonconstant $\chi_e(r)$ radial profiles. However, the similarities in the curves for different $\chi_e(r)$ profiles and the uncertainties in the experimental t_p versus r^2 data make it difficult to infer directly the radial profile of $\chi_e(r)$.

In summary, sawtooth-induced electron temperature perturbations propagate diffusively through the TFTR plasma at a rate which is faster than that expected from equilibrium electron heat transport. Two hypotheses to explain this discrepancy have been proposed: (1) the electron heat diffusivity χ_e varies during the time the heat pulses pass through the plasma; or (2) a "heat pinch" effect nearly cancels the outward heat diffusivity. However, both hypotheses require further study to identify the nature of the time-dependent or additional terms required in Eq. (1) in order to explain the diffusive nature of the heat pulses. Also, the origin of the additional terms needs to be identified. For example, the time varying χ_e might be caused by enhanced magnetic or electrostatic fluctuations associated with a mode which is destabilized by the crash of the sawtooth. It is possible that a resolution

of the discrepancy in χ_e could lead to a better understanding of the process causing anomalous transport in large tokamak plasmas such as TFTR.

9.0 COMPOUND SAWTEETH

A recently observed new phenomenon which has resulted in improved understanding of mechanisms underlying instabilities and of electron thermal diffusivity is the compound sawtooth relaxation. Sawteeth relaxations are so named because of the sawtooth-like signature observed on the line-integrated x-ray emissivity. The XIS and electron cyclotron emission (ECE) system have been the main instruments for studying this phenomenon. These large amplitude long period (τ 250 ms) compound sawteeth have been observed in ohmically heated, high current, high density plasmas in TFTR and JET (1 sec) and in neutral-beam-heated discharges in Doublet III. The fact that compound sawteeth cannot be explained by the Kadomtsev model, invoked as an explanation for normal sawteeth, has spurred new theoretical investigations and intensified experimental studies in an attempt to gain insight into the underlying mechanisms.

"Compound" sawteeth comprise a more complex relaxation phenomenon than do "simple" or "normal" sawteeth /44/. Simple sawteeth consist of a series of periodic oscillations as shown in Fig. 20a around 1 s. Each cycle is characterized by a slow rise of the central temperature, resulting in a gradual increase in central x-ray emissivity, followed by a rapid flattening of the temperature profile [$T_e(r)$] and concurrent rapid decrease in central x-ray emissivity. In simple sawteeth the rapid drop or sawtooth "crash" is immediately preceded by relatively small m=1, n=1 precursor oscillations. Successor oscillations, following the crash, are seldom observed. The sawtooth cycle is interpreted as a slow increase in central heating due to a

centrally peaked current profile, leading to an instability which rapidly expels energy from the center radially outward and flattens the temperature profile in the central region. XIS detectors viewing chords outside the q=1 radius observe a slow decrease in emissivity while the electron temperature profile is peaking, and a rapid increase in emissivity at the sawtooth crash, confirming the rapid outward transport of thermal energy. This inversion is illustrated in Fig. 20b, except for compound sawteeth. Also, Fig. 20c shows normal central and inverted outer T_e traces from ECE measurements. Small sawteeth (Fig. 20a from about 1.7 to 2 s) have small m/n = 1/1 precursor oscillations but have large successors like the main relaxations at the compound sawteeth.

The compound sawtooth cycle begins, as does the simple sawtooth, with a slow peaking of the $T_e(r)$ profile. However, before the main relaxation a "subordinate" relaxation occurs (Fig. 20b and 21 top) /42/. The subordinate relaxation differs from the main relaxation (and from simple sawteeth) in that only a minor flattening of the temperature (Fig. 21 top) and x-ray emission profiles occurs and only over intermediate radii; a very small perturbation occurs at r = 0, but T_e and x-ray emission increases noticeably at the edge. In contrast the main relaxation of the compound sawtooth flattens $T_e(r)$ markedly all the way to the center (Fig. 21 bottom). Furthermore, the subordinate relaxation has small precursor and large successor oscillations. Sometimes the successor oscillations persist for ten's of milliseconds. The main relaxation has very small precursors and medium-amplitude successor oscillations.

The compound sawteeth are not fully understood, but a proposed explanation suggests that the phenomenon results from a flat to hollow current profile and slow current penetration in large high temperature tokamaks.

Theoretical simulations indicate that a flat current profile develops a skin-like current with two q = 1 surfaces. Under these conditions relaxations corresponding to both the subordinate and the main relaxation can occur; the former involves a partial reconnection of magnetic field lines, and the latter involves a complete reconnection that penetrates to the center of the plasma.

10.0 ELECTRON DISTRIBUTION FUNCTION DURING LOWER-HYBRID CURRENT DRIVE

Noninductive current drive provides the potential for steady-state operation of tokamaks, which is desirable for reactor effectiveness. Successful current drive by radio-frequency (rf) driven lower-hybrid waves has been demonstrated in PLT /10-13,45/ and other tokamaks /46,47/. Hard x-ray measurements during lower-hybrid current-drive (LHCD) experiments on PLT have shown the existence of a non-Maxwellian tail of energetic electrons formed by the rf waves. In an attempt to improve understanding of the LHCD physics, one of the main goals of the PLT LHCD experiments has been measurement of the plasma electron distribution function. Toward this goal a hard x-ray diagnostic system has been developed, detailed measurements have been made, and comparison of the data with computer modeling has provided excellent information on the electron distribution. Also, strong evidence for a theoretically predicted instability which causes a transfer from parallel to perpendicular energy has been observed /13/.

Determination of the anisotropic non-Maxwellian portion of the electron distribution function involves measurement of the bremsstrahlung from the high energy electrons. The fact which makes this measurement possible is that the bremsstrahlung is strongly peaked in the direction of electron propagation for electron energies above 50 keV. Thus, a highly collimated detector will respond more to electrons moving parallel to its line of sight than to

perpendicular electrons. Adjustment of the angle of the diagnostic relative to the magnetic field allows a mapping out of the angular distribution of emitted radiation and, thus, acquisition of information about the angular distribution of the electrons. However, the complex x-ray emission processes must be theoretically simulated with model electron distribution functions in order to interpret the data, since (a) both the electrons and photons have a range of energies and anisotropic distributions, (b) the emission spectrum and angular distribution are complex functions of electron energy, and (c) the experimental geometry varies with angle in a complex way.

The instrumentation for measuring the angular distribution of hard x rays and the measurement and modeling results have been discussed in several papers /10-13/. Here we present an overview of the observations, with emphasis on the observed evidence for the Parail-Pogutse instability which results in a sudden relaxation of the energetic electron distribution and a transfer from parallel to perpendicular energy.

Computer modeling has succeeded in reproducing the measured emission reasonably well. The best fit so far has been obtained with a two-step radial variation of the electron distribution function which is less energetic in the interior half of the plasma and more energetic on the outside. This comparison is illustrated in Fig. 22b where the solid lines are simulated emission, and the points are measured data. Parallel and perpendicular components of the electron velocity distribution function are described by factors of the type $\exp(-p^2/2T)$, where p is momentum and T is temperature. Subscripts $\parallel F$ and $\parallel B$ denote "parallel forward" and "parallel backward." E^* is a maximum or cutoff energy. The parameters are $T_{\parallel B}$ equals $T_\perp$ = 150 keV throughout the plasma. However, for $0 < r < 20$ cm, $T_{\parallel F}$ = 750 keV and E^* = 425 keV, whereas for $20 < r < 40$ cm, $T_{\parallel F}$ = 5,000 keV and E^* = 800 keV. The

momentum distribution functions are illustrated in Fig. 22a. The reduced emission for $\theta < 45°$ is caused by the fact that the line of sight passes predominately through the inner region which has less energetic electrons. The assumption of the maximum electron energy $E^* = 425$ keV in the interior is consistent with the lower-hybrid wave accessibility condition, which restricts the waves capable of penetrating to the interior to those with phase velocities which can resonate with electrons at energies less than or equal to 400 keV.

Relaxation oscillations which seem to have the characteristics of the Parail-Pogutse instability have also been observed during LHCD experiments with the tangential hard x-ray system /37/. The data are illustrated in Fig. 23 and show that there is a transfer from parallel to perpendicular energies accompanying these relaxations. The two traces represent the total hard x-ray intensity emitted perpendicular (90 degrees) and near parallel (28 degrees) to the direction of the lower-hybrid waves. For these measurements the pulses from the NaI detector were integrated by a 10-kHz low-pass filter, and the apertures were opened to maximum size to optimize statistics (current mode).

Under normal current drive conditions, (Fig. 23a) a single small relaxation occurs shortly after the rf is turned off. The decrease in parallel intensity and increase in perpendicular intensity demonstrates that parallel energy is converted into perpendicular energy and supports the view that the relaxation instability is due to the anomalous Doppler effect. Also, in Fig. 23a both parallel and perpendicular intensities increase when the rf is turned on and saturate shortly afterwards. As the rf power is decreased, the electric field in the plasma probably increases. This is consistent with the observation in Fig. 23b; i.e., the parallel intensity does not saturate, but continues to increase, and the instability amplitude or transfer of energy

from parallel to perpendicular is greater. Both of these observations suggest an acceleration of electrons to higher and higher parallel energies. In Fig. 23c, at still lower rf power, the parallel energy increases even more rapidly and the relaxation actually occurs before the rf is turned off. Figures 23a-c were for a plasma density of 5×10^{12} cm^{-3}. Figure 23d, however, is at higher electron density, where the rf current drive is less efficient. Thus, even though the rf power is high as in Fig. 23a, this case has the characteristics of the weak current-drive data of Fig. 23c.

ACKNOWLEDGMENTS

The authors gratefully acknowledge the continuing support of Drs. H.P. Furth, P.H. Rutherford, D.J. Grove, D.M. Meade, and K.M. Young. Appreciation is expressed to J. Rice, R. Petrasso, and M. Dubois for providing figures from their experimental work. Figures from Ref. 2-7 and 20 were used with permission from the journal editors. This work was supported by U.S. DoE Contract No. DE-AC02-76-CHO-3073.

REFERENCES

/1/ HILL, K.W., et al., "Tokamak X-Ray Diagnostic Instrumentation,", Proc. of Course and Workshop on Basic and Advanced Fusion Plasma Diagnostic Techniques, Varenna, Italy, September 1986, to be published.

/2/ HILL, K.W, BITTER, M., BRETZ, N.L., DIESSO, M., EFTHIMION, P.C., VON GOELER, S., KIRALY, J., RAMSEY, A.T., SAUTHOFF, N.R., SCHIVELL, J., and SESNIC, S., Nucl. Fusion 26, 1131 (1986).

/3/ PETRASSO, R.D., WENZEL, K.W., HOPF, J.E., SIGMAR, D.J., GREENWALD, M., TERRY, J.L., and PARKER, J., Phys. Rev. Lett. 57 (1986) 707.

/4/ LA FONTAINE, A. COMPANT, DUBOIS, M.A., PECQUET, A.L., BOYD, D.A., CAVALLO, A., COHEN, S.A., VON GOELER, S., HULSE, R.A., MANOS, D.M., SMITH, R., and WILSON, R., Plasma Phys. Contr. Fus. 27 (1985) 229.

/5/ BITTER, M., HILL, K.W., ZARNSTORFF, M., VON GOELER, S., HULSE, R., JOHNSON, L. C., SAUTHOFF, N.R., SESNIC, S., YOUNG, K.M., TAVERNIER, M., BELY-DUBAU, F., FAUCHER, P., CORNILLE, M., and DUBAU, J., Phys. Rev. A32 (1985) 3011.

/6/ BEIERSDORFER, P., BITTER, M., VON GOELER, S., COHEN, S., HILL, K.W., TIMBERLAKE, J., WALLING, R.S., CHEN, M.H., HAGELSTEIN, P.L., and SCOFIELD, J.H., Phys. Rev. A34 (1986) 1297.

/7/ RICE, J.E., MARMAR, E.S., TERRY, J.L., KÄLLNE, E., and KÄLLNE, J., Phys. Rev. Lett. 56 (1986) 50.

/8/ FREDRICKSON, E. et al., Nucl. Fus. 26 (1986) 849.

/9/ YAMADA, H., MCGUIRE, K., COLCHIN, R.J., EFTHIMION, P.C., FREDRICKSON, E., HILL, K.W., KIRALY, J., PARE, V., TAYLOR, G., and SAUTHOFF, N.R., Princeton Plasma Physics Laboratory Report PPPL-2213 (September 1985).

/10/ VON GOELER, S., STEVENS, J., BERNABEI, S., BITTER, M., CHU, T.K., EFTHIMION, P., FISCH, N., HOOKE, W., HILL, K., HOSEA, J., JOBES, F., KARNEY, C., MERVINE, J., MESERVEY, E., MOTLEY, R., RONEY, P., SESNIC, S., SILBER, K., and TAYLOR, G., Nucl. Fusion 25 (1985) 1515.

/11/ STEVENS, J., VON GOELER, S., BERNABEI, S., BITTER, M., CHU, T.K., EFTHIMION, P., FISCH, N., HOOKE, W., HOSEA, J., JOBES, F., KARNEY, C., MESERVEY, E., MOTLEY, R., and TAYLOR, G., Nucl. Fus. 25, (1985) 1529.

/12/ VON GOELER, S., STEVENS, J.E, STODIEK, W., BERNABEI, S., BITTER, M., CHU, T.K., HILL, K.W., HILLIS, D., HOOKE, W.M., JOBES, F.C., LENNER, G., MESERVEY, E.B., MOTLEY, R.W., SAUTHOFF, N.R., SESNIC, S., and TENNEY, F.H., in proceedings of the Course on Diagnostics for Fusion Reactor Conditions, Varenna, Italy, September 1982 (Pergamon, New York, 1983), Vol. I, 87.

13/ VON GOELER, S., STEVENS, J.E., KARNEY, C.F.F., BERNABEI, S., BITTER, M., CHU, T.K., EFTHIMION, P.C., HILL, K.W., HOOKE, W.M., JOBES, F.C., MAZZUCATO, E., MESERVEY, E.B., MOTLEY, R.W., RONEY, P., SAUTHOFF, N.R., SESNIC, S., TAYLOR, G., TENNEY, F.H., and VALEO, E.J., in proceedings 5th Topical Conference on Radio-Frequency Heating, Madison, WI, 82 (1983) 96.

/14/ ENGELHARDT, W. et al., in Proceedings 7th International Conference on Plasma Physics and Controlled Nuclear Fusion Research, Innsbruck, 1978, (IAEA, Vienna 1979) Vol. I, 123.

/15/ RAMSEY, A.T., HILL, K.W., BITTER, M., BOODY, F.P., BUSH, C.E., DYLLA, H.F., FONCK, R.J., VON GOELER, S., GREK, B., MANOS, D.M., JOHNSON, D.W., SESNIC, S., STRATTON, B.C., and TAYLOR, G., 7th International Conference on Plasma-Surface Interactions in Controlled Fusion Devices ,Princeton, NJ, 5-9 May 1986; J. Nucl. Materials 145-146 (1987).

/16/ DYLLA, H.F. et al., Ibid.; in J. Nucl. Materials 145-146 (1987).

/17/ MCCRACKEN, G.M., STOTT, P.E., Nucl. Fusion 19 (1979) 889.

/18/ EFTHIMION, P.C. et al., in proceedings 10th International Conference on Plasma Physics and Controlled Nuclear Fusion Research, London, UK, 1984, (IAEA, Vienna, 1985) Vol. I, 29.

/19/ HILL, K.W., BITTER, M., DIESSO, M., DUDEK, L., VON GOELER, S., HAYES, S., JOHNSON, L.C., KIRALY, J., MOSHEY, E., RENDA, G., SESNIC, S., SAUTHOFF, N.R., TENNEY, F., and YOUNG, K.M., Rev. Sci. Instrum. 56 (1985) 840.

/20/ SILVER, E.H., BITTER, M., BRAU, K., EAMES, D., GREENBERGER, A., HILL, K. W., MEADE, D.M., RONEY, W., SAUTHOFF, N.R., and VON GOELER, S., Rev. Sci. Instrum. 56 (1985) 1198.

/21/ HILL, K.W. et al., Rev. Sci. Instrum. 57 (1986) 2151.

/22/ STRATTON, B.C., private communication.

/23/ BELL, M.G., et al., 13th European Conference on Controlled Fusion and Plasma Heating, Schliersee, FRG, April 14-18, 1986; to be published in proceedings.

/24/ HILL, K.W. et al., Bull. Am. Phys. Soc. 30 (1985) 1521.

/25/ KILPATRICK, S.J. et al., Princeton University, Plasma Physics Laboratory Report PPPL-2284 (1986).

/26/ RUTHERFORD, P.H. et al., Princeton University Plasma Physics Laboratory Report PPPL-1297 (1976).

/27/ SESNIC, S., et al., 7th International Conference on Plasma-Surface Interactions in Controlled Fusion Devices, Princeton, NJ, May 1986; J. Nucl. Materials 145-146 (1987).

/28/ IDA, K. et al., Princeton University Plasma Physics Laboratory Report PPPL-2313 (1986); Phys. Rev. Lett. 58, 116 (1987).

/29/ SEGUIN, F.H., PETRASSO, R., MARMAR, E.S., Phys. Rev. Lett. 51 (1983) 455.

/30/ IDA, K. et al., Princeton University Plasma Physics Laboratory Report PPPL-2264 (1985); Plasma Physics and Controlled Fusion 28, 879 (1986).

/31/ HILL, K.W., BITTER, M., TAVERNIER, M., DIESSO, M., VON GOELER, S., JOHNSON, G., JOHNSON, L.C., SAUTHOFF, N.R., SCHECHTMAN, N., SESNIC, S., TENNEY, F.H., and YOUNG, K.I , Rev. Sci. Instrum. 56 (1985) 1165.

/32/ BARTIROMO, R., in proceedings Workshop on Diagnostics for Fusion Reactor nditions, Varenna, Italy, September 1982 (Pergamon, New York, 1983) 123.

/33/ KÄLLNE, E., KÄLLNE, J., and RICE, J.E., Phys. Rev. Lett. 49 (1982) 330.

/34/ BITTER, M., VON GOELER, S., HORTON, R., GOLDMAN, M., HILL, K.W., SAUTHOFF, N.R., and STODIEK, W., Phys. Rev. Lett. 42 (1979) 304.

/35/ HILL, K.W., BITTER, M., GOLDMAN, M., SAUTHOFF, N.R., and VON GOELER, S., Bull. Am. Phys. Soc. 26 (1984) 864.

/36/ WONG, K.L., BITTER, M., HAMMETT, G.W., HEIDBRINK, W., HENDEL, H.W., et al., Phys. Rev. Lett. 55 (1985) 2587; BITTER, M., SCOTT, S.D, WONG, K.L., GOLDSTON, R.J., GREK, B., VON GOELER, S., HAWRYLUK, R.J., HILL, K.W., HSUAN, H., JOHNSON, D.W.,SESNIC, S., TAIT, G.D, and ZARNSTORFF, M.C., Princeton Plasma Physics Laboratory Report PPPL-2357 (1986); submitted to Nucl. Fusion.

/37/ HILL, K.W., VON GOELER, S., BITTER, M., CAMPBELL, L., COWAN, R.D., FRAENKEL, B., GREENBERGER, A., HORTON, R., HOVEY, J., RONEY, W., SAUTHOFF, N.R., and STODIEK, W., Phys. Rev. A19 (1979) 1770.

/38/ VON GOELER, S., HILL, K.W., BITTER, M., CLIFFORD, C., FREDD, E., GOLDMAN, M., JOHNSON, L.C., KU, L.P., MOSHEY, E., RENDA, G., SAUTHOFF, N.R., SESNIC, S., TENNEY, F.H., and YOUNG, K.M., proceedings of the Course on Diagnostics for Fusion Reactor Conditions, Varenna, Italy, September 1982 (Pergamon, New York, 1983) Vol. I, 69.

/39/ BELY-DUBAU, F., FAUCHER, P., STEEMAN-CLARK, L., BITTER, M., VON GOELER, S., HILL, K.W., CAMHY-VAL, C., and DUBAU, J., Phys. Rev. A26 (1982) 3459.

/40/ BELY-DUBAU, F., BITTER, M., DUBAU, J., FAUCHER, P., GABRIEL, A.H., HILL, K.W., VON GOELER, S., SAUTHOFF, N.R., and VOLONTE, S., Phys. Lett. 93A (1983) 189.

/41/ JAHNS, G.L., SOLER, M., WADDELL, B.V., CALLEN, J.D., and HICKS, H.R, Nucl. Fusion 18 (1978) 609.

/42/ TAYLOR, G., et al., Nucl. Fusion 26 (1986) 339.

/43/ SOLER, M. and CALLEN, J.D., Nucl. Fusion 19 (1979) 703.

/44/ MCGUIRE, K., et al., in proceedings 12th European Conf. on Controlled Fusion and Plasma Physics, Budapest, September 1985, Vol. I, 134.

/45/ BERNABEI, S. et al., Phys. Rev. Lett. 49 (1982) 1255.

/46/ DEMARCO, F., proceedings Course and Workshop on Applications of RF Waves to Tokamak Plasmas, Varenna, Italy, September 1985 (Monotypia Franchi, CiHa di Castello, Italy, 1985) Vol. I, 316.

/47/ PORKOLAB, M. et al., proceedings Fifth Topical Conference on Radio-Frequency Plasma Heating (University of Wisconsin, Madison, WI, February 1983, B2) p. 88.

FIGURE CAPTIONS

Fig. 1. Density dependence of metal concentrations in TFTR measured by the x-ray pulse-height analyzer (PHA) for several plasma currents. Curves are for titanium with a TiC-coated graphite limiter and total metals (Cr, Fe, and Ni) for two graphite limiters. (Note different scales).

Fig. 2. Central Z_{eff} in TFTR measured by the PHA for two graphite limiter configurations.

Fig. 3. Density dependence of central nickel concentration in TFTR for different degrees of conditioning of the graphite or TiC-coated graphite limiter. The nickel concentration decreased with the number N of shots since pulse discharge cleaning as $N^{-0.6}$.

Fig. 4. Enhancement of nickel and low-Z impurities in TFTR with heating power (ohmic plus neutral beams) relative to ohmic heating only, at the same density and current.

Fig. 5. (a) and (b) X-ray signals from five chords of an array sensitive to Mo radiation. Top signal is center, and the chords are 1.7 cm apart. (c) X-ray emission profiles. (PPPL 86X3237)

Fig. 6. Radial profiles just before (i) and (ii) after the large impurity disruption. (a) carbon density, (b) Mo density, (c) electron density, (d) electron temperature, (e) hydrogen density, and (f) Spitzer conductivity. (86X3236)

Fig. 7. Time evolution of the central chord soft x-ray signal from PLT during a discharge with aluminum injection.

Fig. 8. Summary of central chord ultrasoft and soft x-ray signals and central temperature in the Al-injection experiment. (86X3230)

Fig. 9. Doppler broadened and shifted profiles of resonance Kα line of Ti XXI measured by the XCS, inferred (central) ion temperature, and toroidal rotation velocity with 3.6 MW of D° beam heating in TFTR. Other parameters are I_p = 0.7 MA, a = 0.82 m, and maximum $\bar{n}_e$ = 0.85 × 10^{13} cm^{-3}.

Fig. 10. (a) Measured (points) and synthetic (solid curve) Kα spectrum of Ti XXI and satellite lines from TFTR recorded by the XCS. (b)-(d) Contributions of various processes to the spectrum. The dotted areas in (c) correspond to Voigt function fits to the data.

Fig. 11. Comparison of ratios of Ti XXI lines measured from TFTR (points) with calculations. Dashed lines include contributions from excitation to $n \geq 3$ followed by cascading and from ionization of Ti XX.

Fig. 12. Grotrian diagram of some energy levels and transitions in Ag^{+37}. Dashed lines at left are x-ray laser transitions. Notation is jj coupling $(j_1, j_2)_j$, where j is angular momentum.

Fig. 13. Selected region of Ag^{+37} n = 3-2 spectrum with other impurity lines subtracted out for clarity. A theoretical spectrum for Na-like (solid lines and lower case letters) and Mg-like (dashed lines and numbers) Ag is shown below.

Fig. 14. Overview of spectra in wavelength range 3.3 - 4.1 Å (first order) and 1.65 - 2.05 Å (second order) showing overlap of calibration bands (shaded) with silver spectral lines.

Fig. 15. X-ray spectra of Ar^{+16} for transitions $1s^2$ - 1snp with n = 7-12 from three chords of Alcator C. Transitions for n = 9 and 10 are enhanced for outer chords due to charge-transfer population of the upper level. (86X3232)

Fig. 16. Comparison of radial profile of neutral hydrogen density deduced from enhancement of peaks shown in Fig. 15 with calculations of neutral transport code FRANTIC. (86X3234)

Fig. 17. Comparison of χ_e's determined by phase shift analysis of heat-pulse propagation with those determined from power balance.

Fig. 18. Plot of inverted soft x-ray sawtooth time-to-peak t_p versus r^2 to determine χ_e. Solid line corresponds to normal sawteeth; dashed for "event" at onset of sawteeth.

Fig. 19. Comparison of temperature perturbation from electron cyclotron emission radiometers at r = 47 cm with predicted temporal behavior from analytic (pulse-shape) solution of heat-pulse-propagation equation.

Fig. 20. (a) Soft x-ray (SX) signals from central chord of TFTR; (b) Expanded SX signals from chords at r = 0 and 37 cm showing normal and inverted compound sawteeth; (c) Electron temperature at positions corresponding to (b).

Fig. 21. (Top) Inverted and normal compound sawteeth of TFTR soft x-ray signals at r = 0.5 and 0 m. (Bottom) Partial flattening of temperature profile (curve B) at intermediate radii after subordinate disruption and complete flattening of central T_e profile (curve D) after main disruption.

Fig. 22. (a) Two-step radial variation of tail distribution function. Parameters for the two distributions are given in the text. (b) Comparison of calculated bremsstrahlung emission (lines) with that measured from PLT (points) versus observation angle for four values of photon energy.

Fig. 23. (a) and (b) Relaxation instability on PLT as seen on near forward (28°) and perpendicular (90°) hard x-ray emission. (a)-(c) Behavior of instability for different levels of rf power. (d) Behavior near high density limit of current drive.

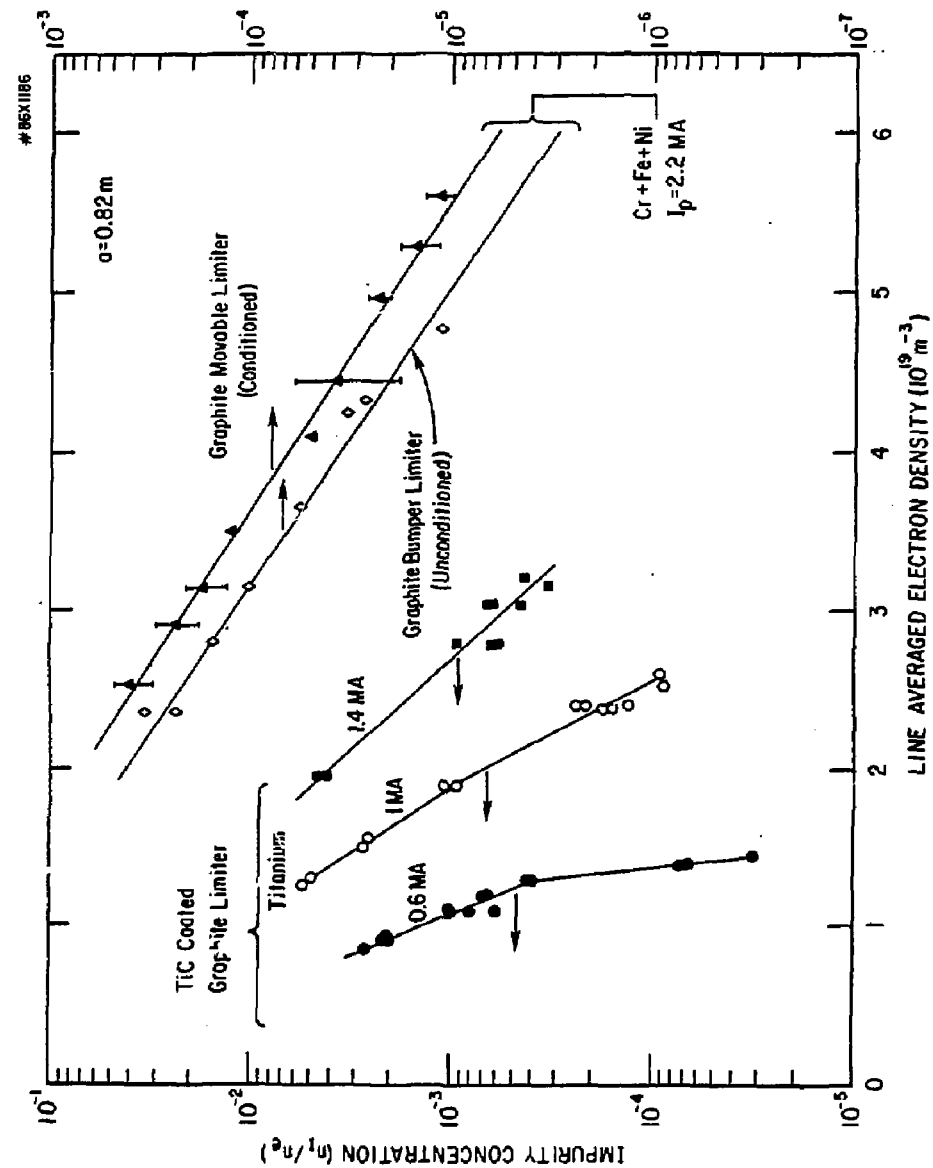
#86X1186
a=0.82 m
Graphite Movable Limiter
(Conditioned)
Graphite Bumper Limiter
(Unconditioned)
Cr+Fe+Ni
I_p=2.2 MA
1.4 MA
1 MA
0.6 MA
TiC Coated
Graphite Limiter
Titanium
IMPURITY CONCENTRATION (n_I/n_e)
LINE AVERAGED ELECTRON DENSITY (10^{19} m^{-3})

Fig. 1

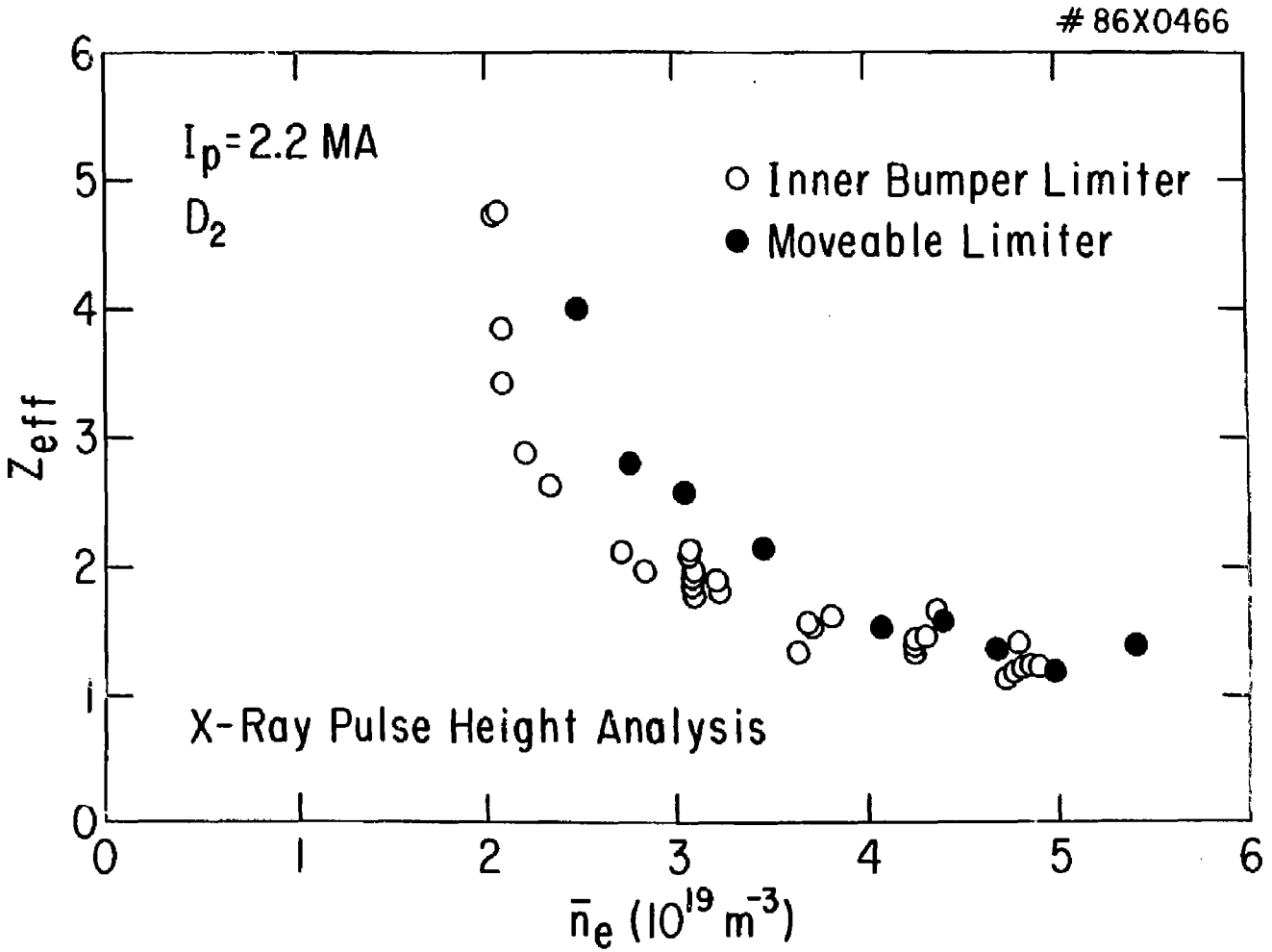
#86X0466
I_p=2.2 MA
D_2
○ Inner Bumper Limiter
● Moveable Limiter
X-Ray Pulse Height Analysis
Z_{eff}
$\bar{n}_e$ (10^{19} m^{-3})
0
1
2
3
4
5
6

Fig. 2

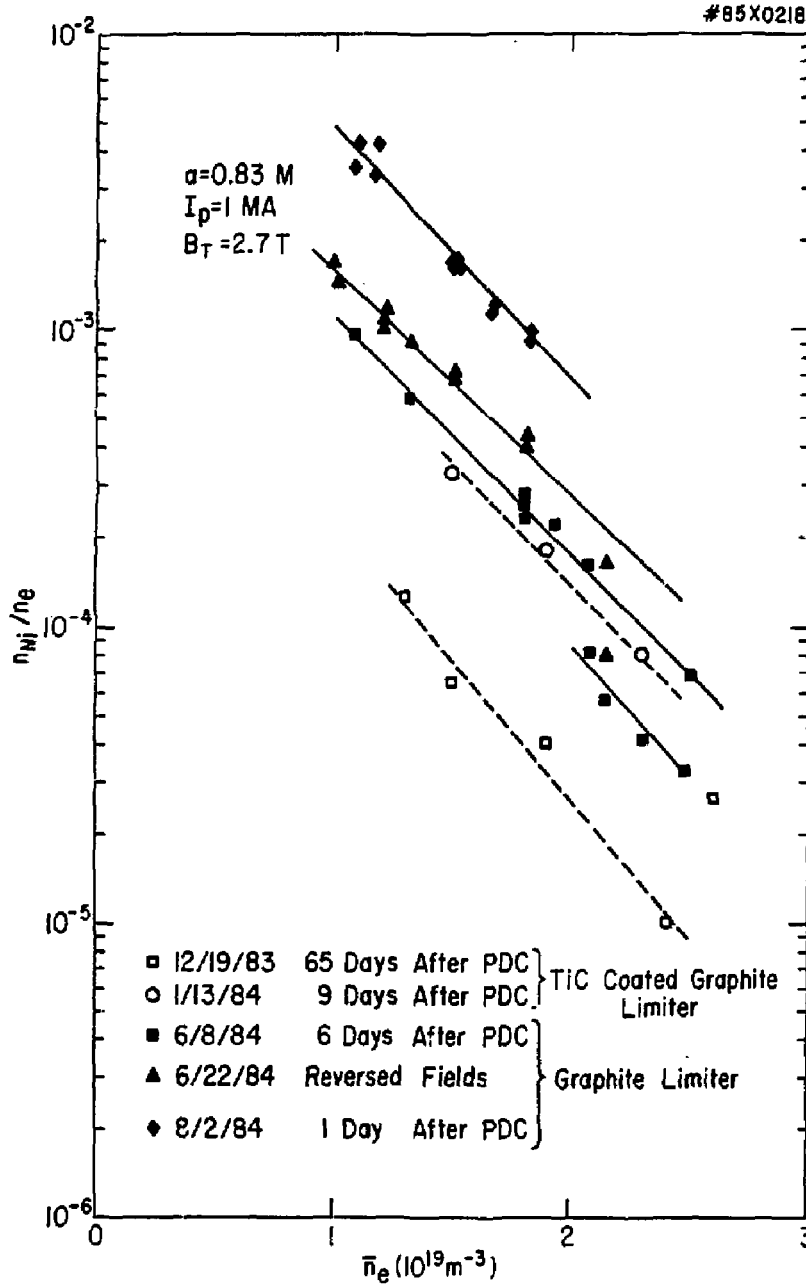
#85X0218
a=0.83 M
I_p=1 MA
B_T=2.7 T
n_{Ni}/n_e
$\bar{n}_e$ (10^{19}m^{-3})
12/19/83 65 Days After PDC
1/13/84 9 Days After PDC
TiC Coated Graphite Limiter
6/8/84 6 Days After PDC
6/22/84 Reversed Fields
8/2/84 1 Day After PDC
Graphite Limiter

Fig. 3

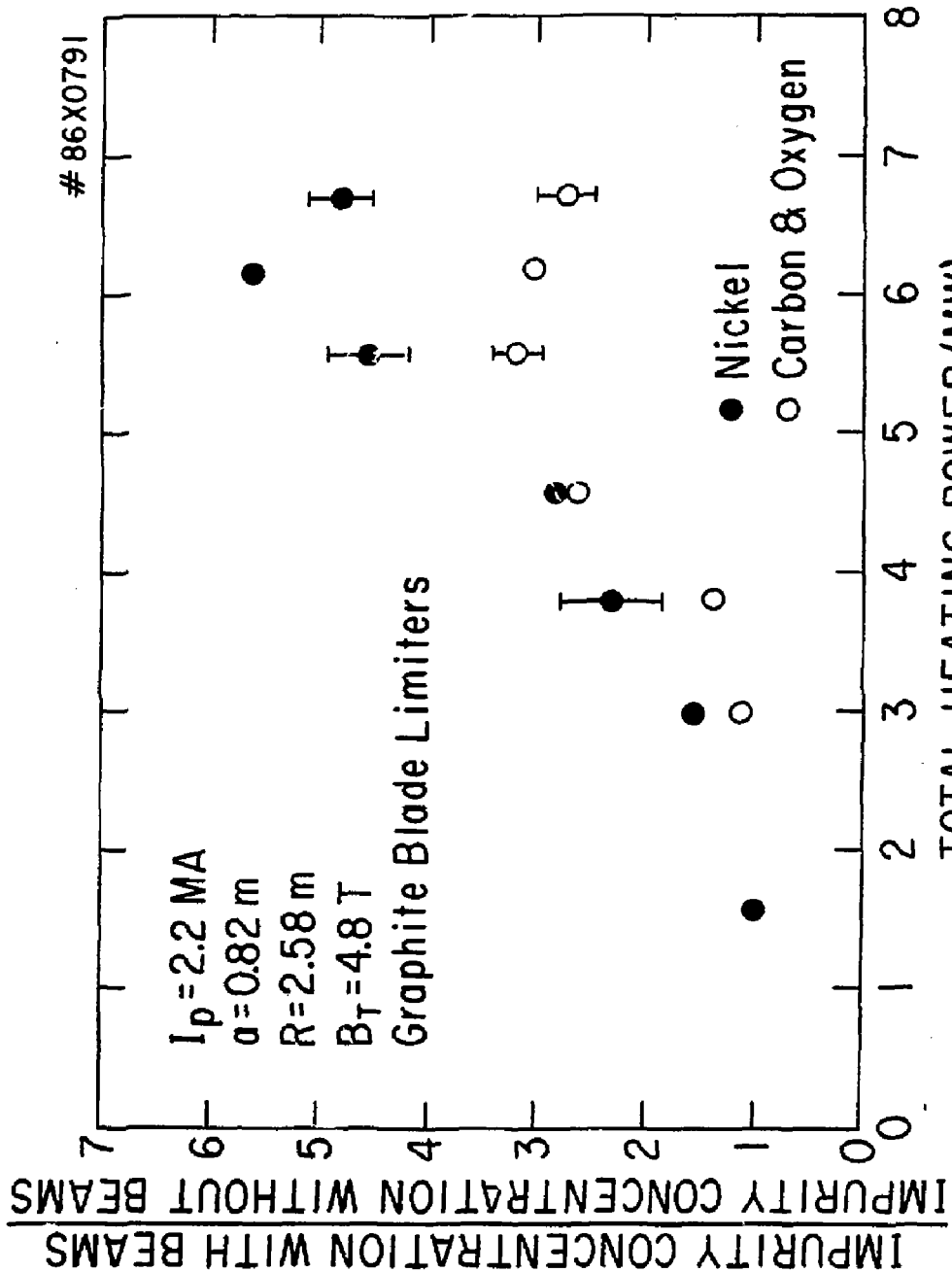
#86X0791
IMPURITY CONCENTRATION WITHOUT BEAMS
IMPURITY CONCENTRATION WITH BEAMS
TOTAL HEATING POWER (MW)
Nickel
Carbon & Oxygen
I_p=2.2 MA
a=0.82 m
R=2.58 m
B_T=4.8 T
Graphite Blade Limiters

Fig. 4

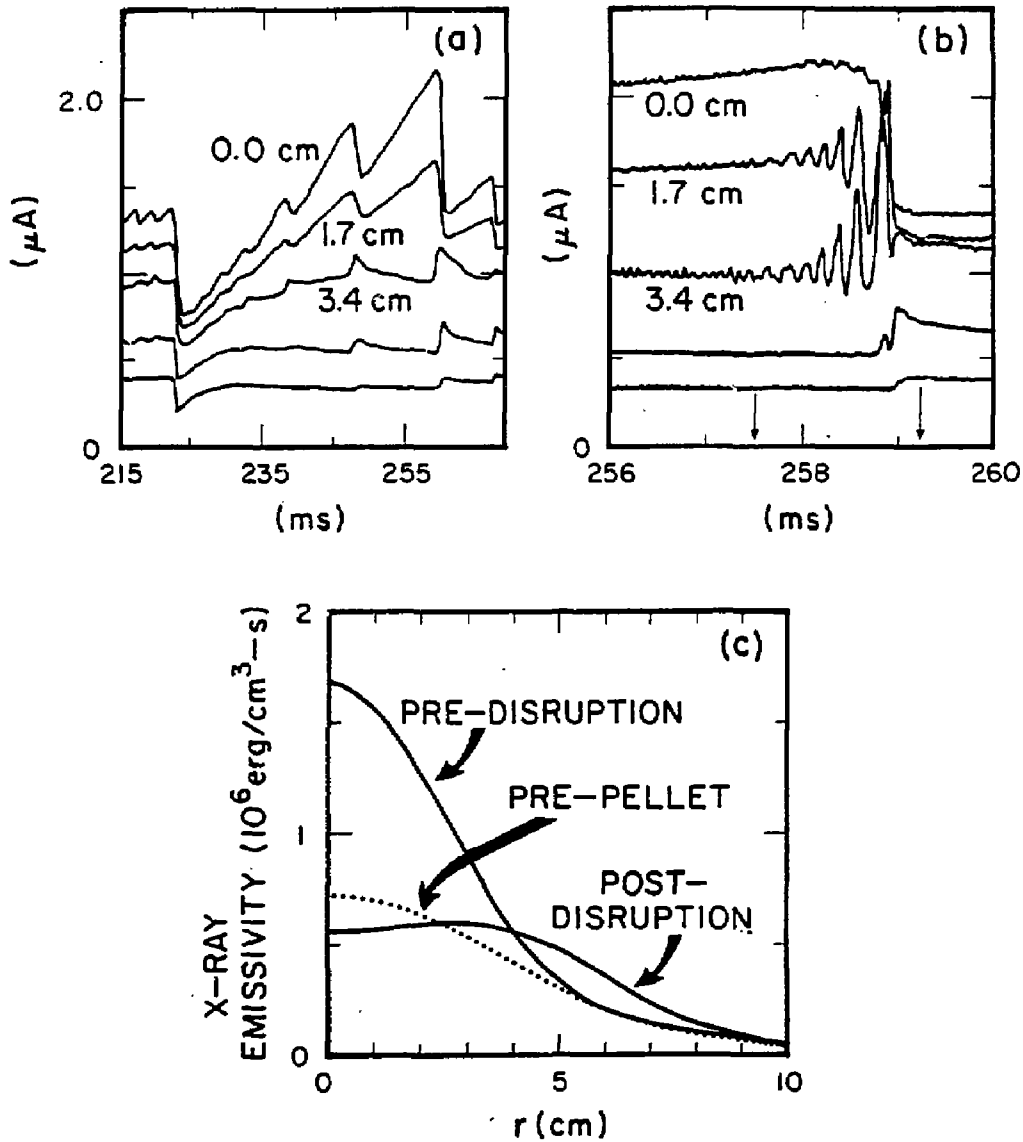
(a)
2.0
0.0 cm
1.7 cm
3.4 cm
(μA)
0
215
235
255
(ms)
(b)
0.0 cm
1.7 cm
3.4 cm
(μA)
0
256
258
260
(ms)
(c)
2
1
0
PRE-DISRUPTION
PRE-PELLET
POST-
DISRUPTION
X-RAY
EMISSIVITY (10^6 erg/cm^3-s)
0
5
10
r (cm)

Fig. 5

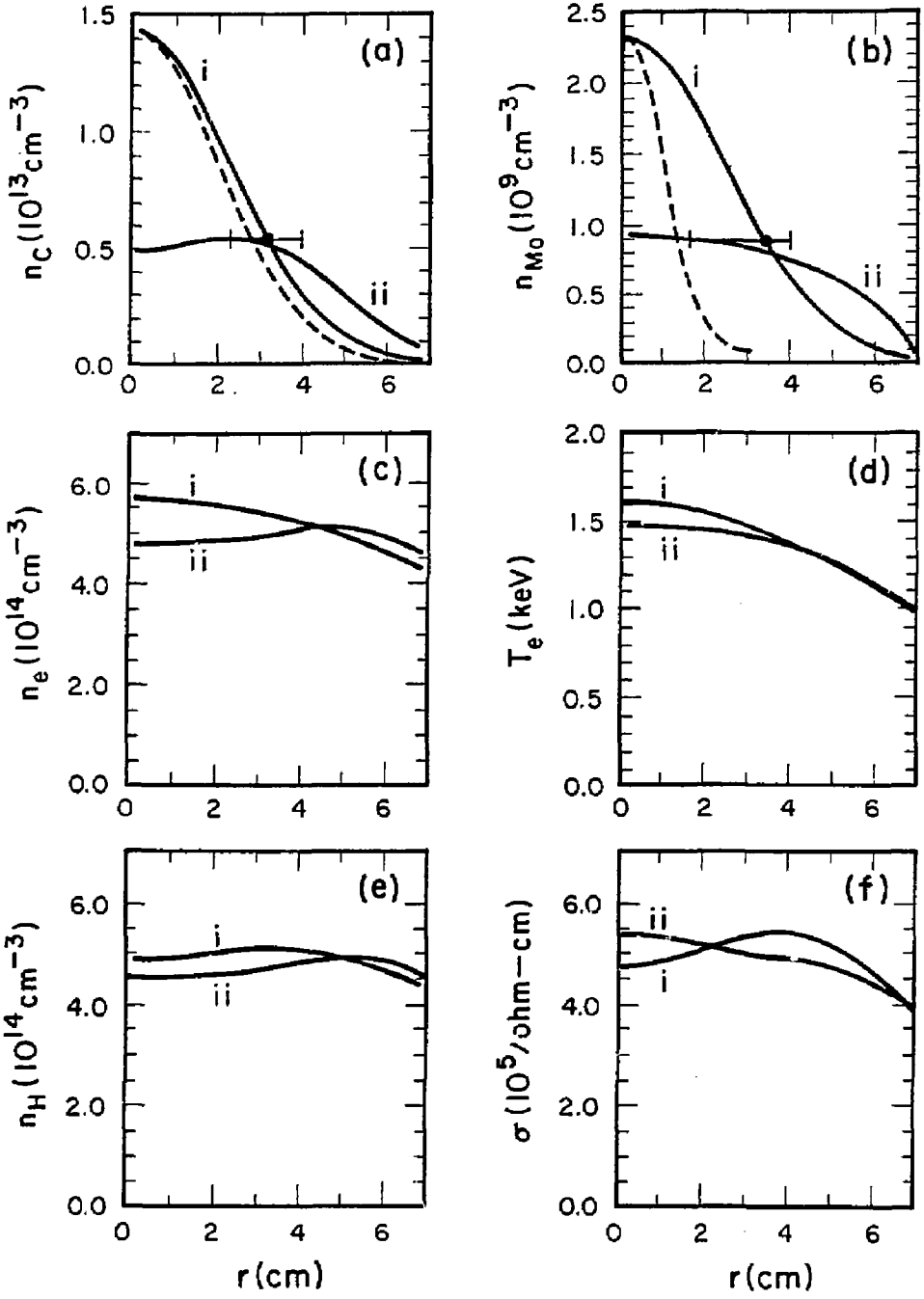
(a)
(b)
(c)
(d)
(e)
(f)
i
ii
$n_C(10^{13}cm^{-3})$
$n_{Mo}(10^9cm^{-3})$
$n_e(10^{14}cm^{-3})$
T_e (keV)
$n_H(10^{14}cm^{-3})$
$\sigma(10^5/ohm-cm)$
r(cm)
r(cm)

Fig. 6

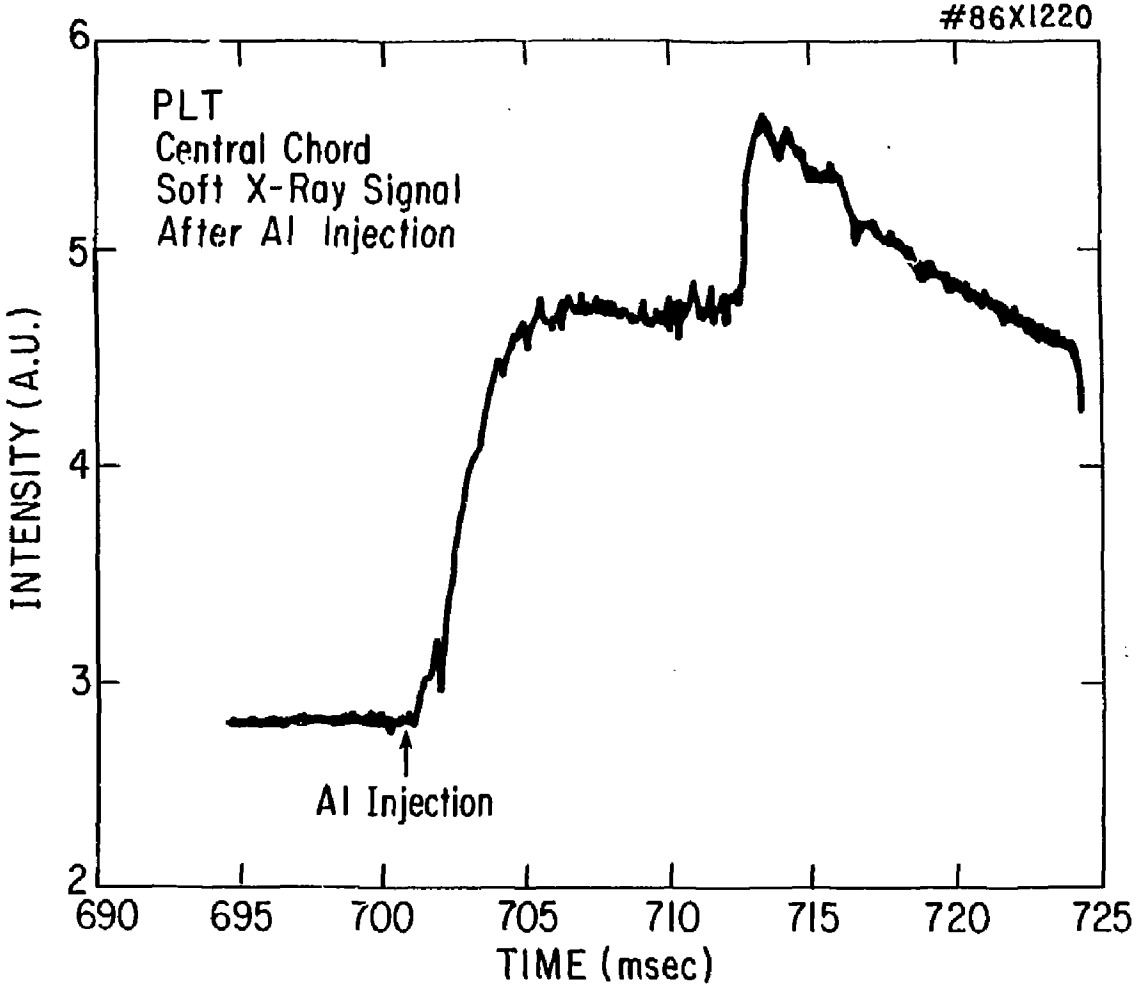
#86X1220
PLT
Central Chord
Soft X-Ray Signal
After Al Injection
INTENSITY (A.U.)
TIME (msec)
Al Injection
6
5
4
3
2
690
695
700
705
710
715
720
725

Fig. 7

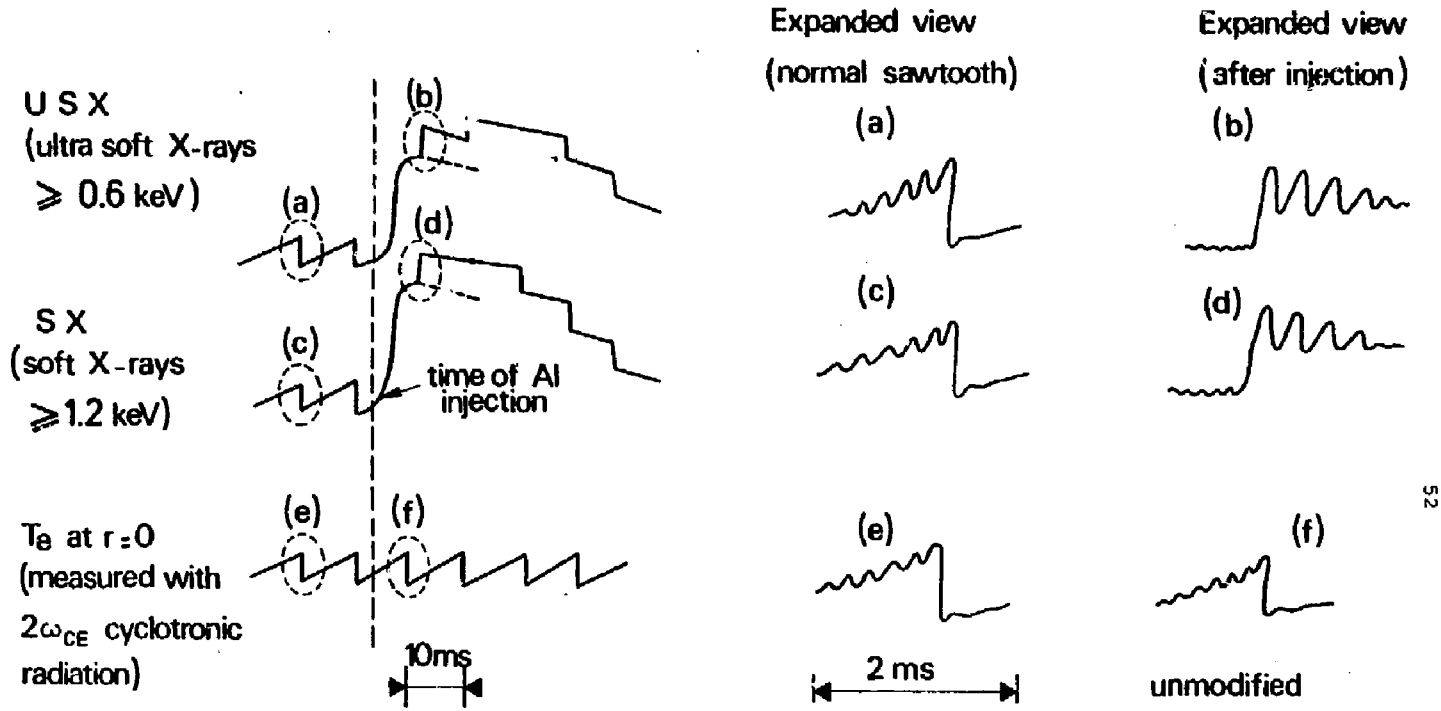
U S X
(ultra soft X-rays
≥ 0.6 keV)
S X
(soft X-rays
≥1.2 keV)
Te at r=0
(measured with
2ωce cyclotronic
radiation)
(a)
(b)
(c)
(d)
(e)
(f)
time of Al
injection
10ms
Expanded view
(normal sawtooth)
Expanded view
(after injection)
2 ms
unmodified

Fig. 8

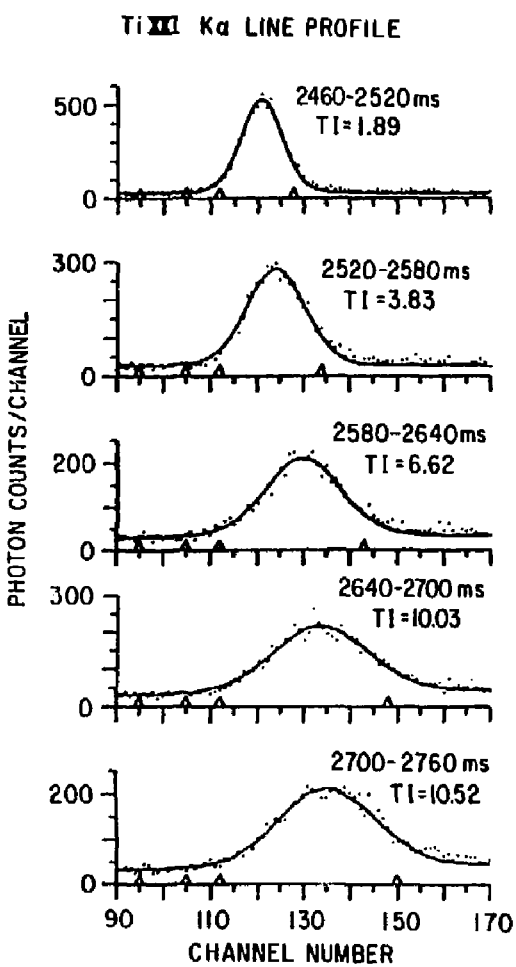
Ti XXI Kα LINE PROFILE
2460-2520ms
TI=1.89
2520-2580ms
TI=3.83
2580-2640ms
TI=6.62
2640-2700ms
TI=10.03
2700-2760ms
TI=10.52
PHOTON COUNTS/CHANNEL
CHANNEL NUMBER

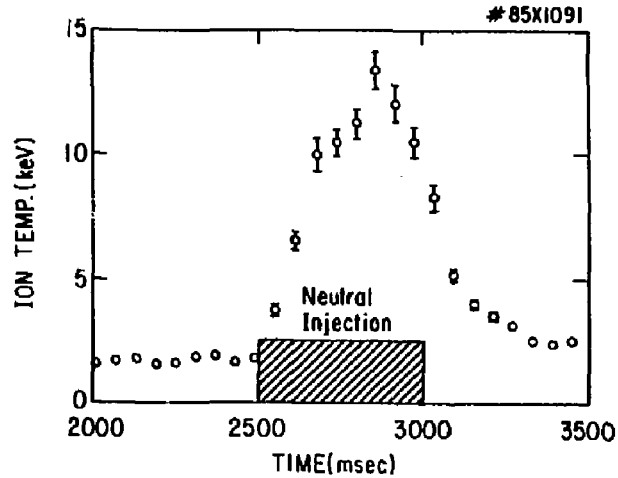
#85X1091
ION TEMP.(keV)
Neutral Injection
TIME(msec)

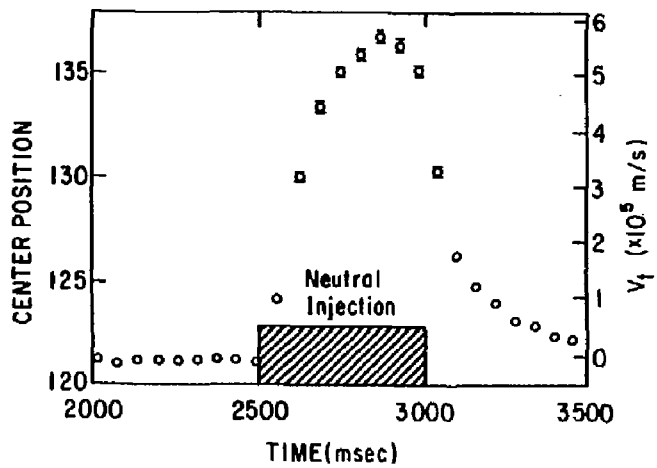
CENTER POSITION
Neutral Injection
TIME(msec)
V_t (x10^5 m/s)

Fig. 9

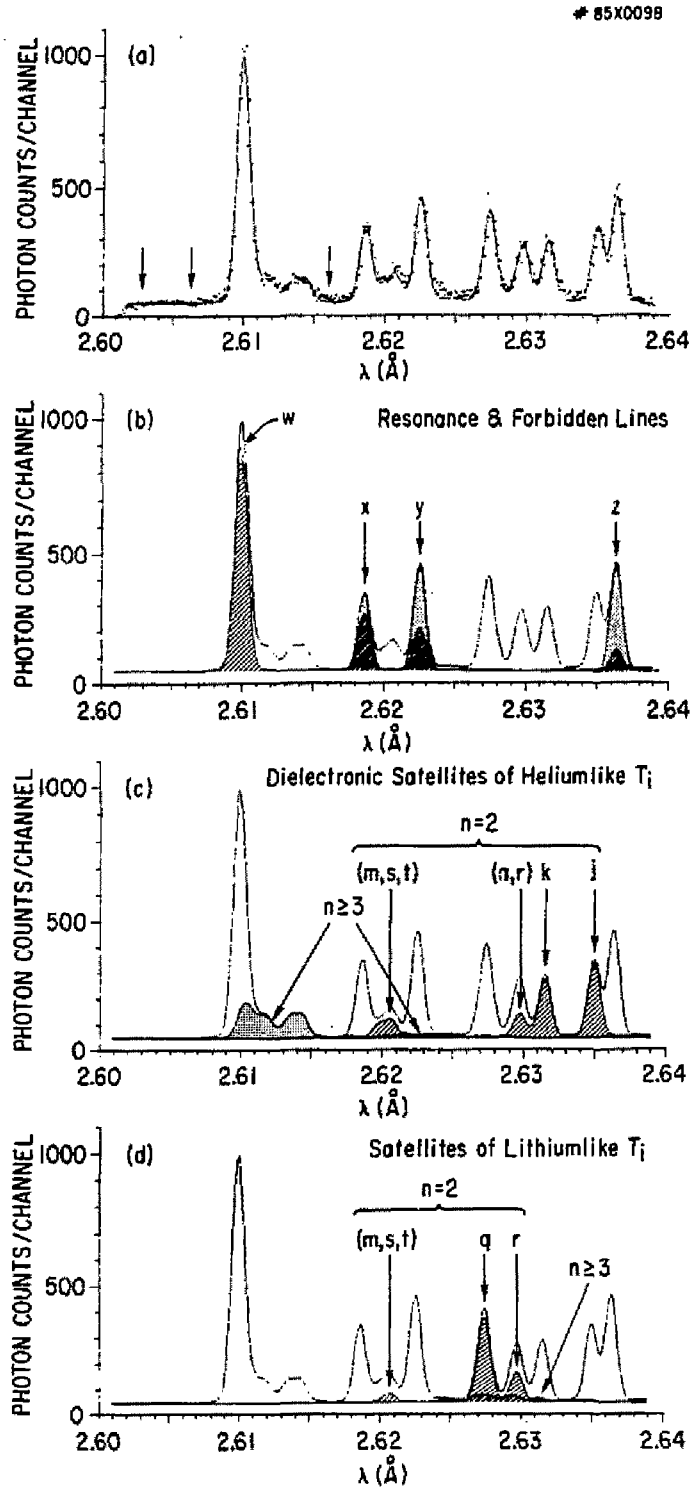
#85X0098
(a)
PHOTON COUNTS/CHANNEL
1000
500
0
2.60
2.61
2.62
2.63
2.64
λ (Å)
(b)
Resonance & Forbidden Lines
w
x
y
z
(c)
Dielectronic Satellites of Heliumlike Ti
n=2
(m,s,t)
(n,r) k
j
n≥3
(d)
Satellites of Lithiumlike Ti
n=2
(m,s,t)
q
r
n≥3

Fig. 10

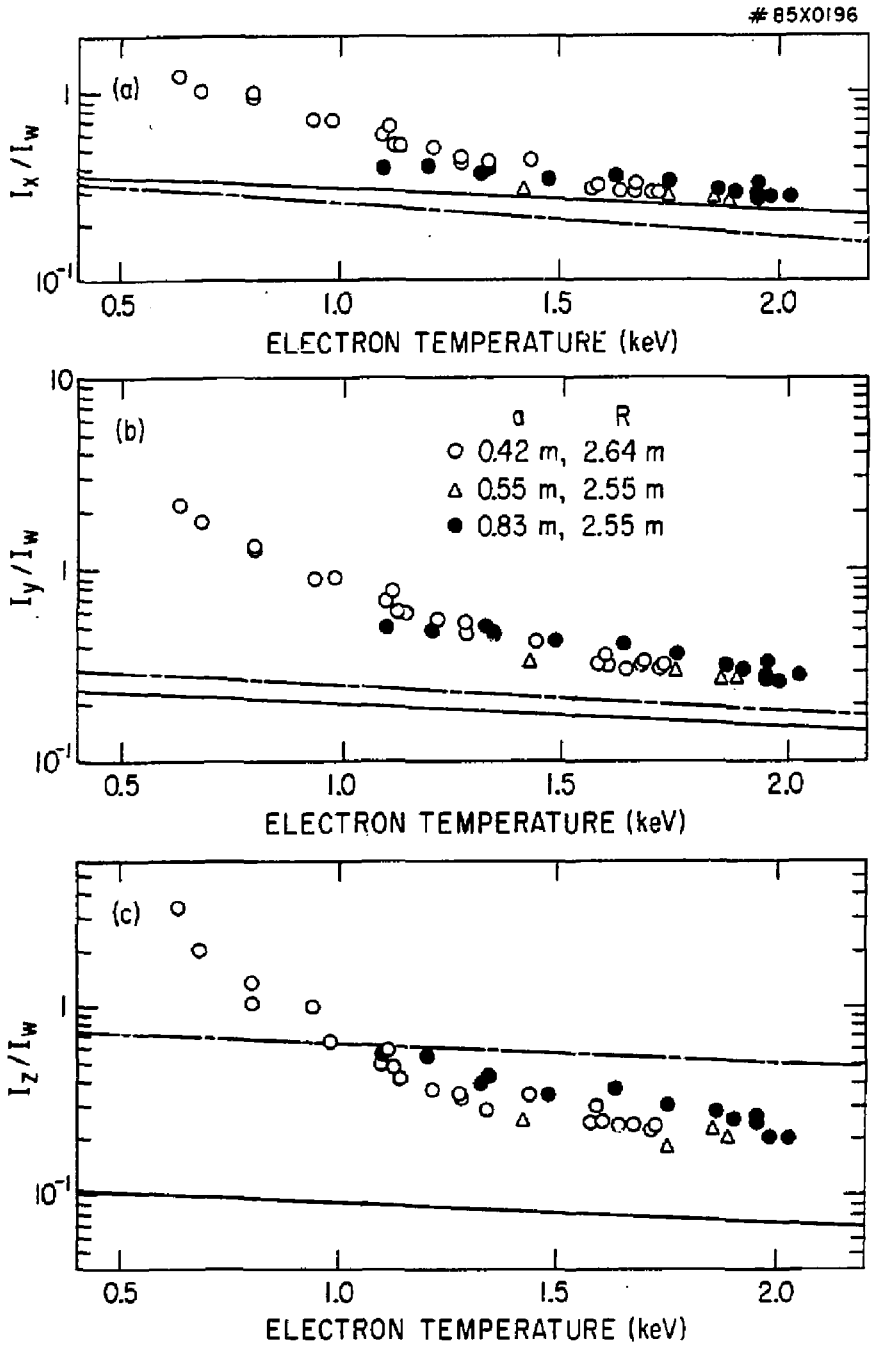
#85X0196
(a)
I_x/I_w
1
10^{-1}
0.5
1.0
1.5
2.0
ELECTRON TEMPERATURE (keV)
(b)
I_y/I_w
10
a R
○ 0.42 m, 2.64 m
△ 0.55 m, 2.55 m
● 0.83 m, 2.55 m
ELECTRON TEMPERATURE (keV)
(c)
I_z/I_w
ELECTRON TEMPERATURE (keV)

Fig. 11

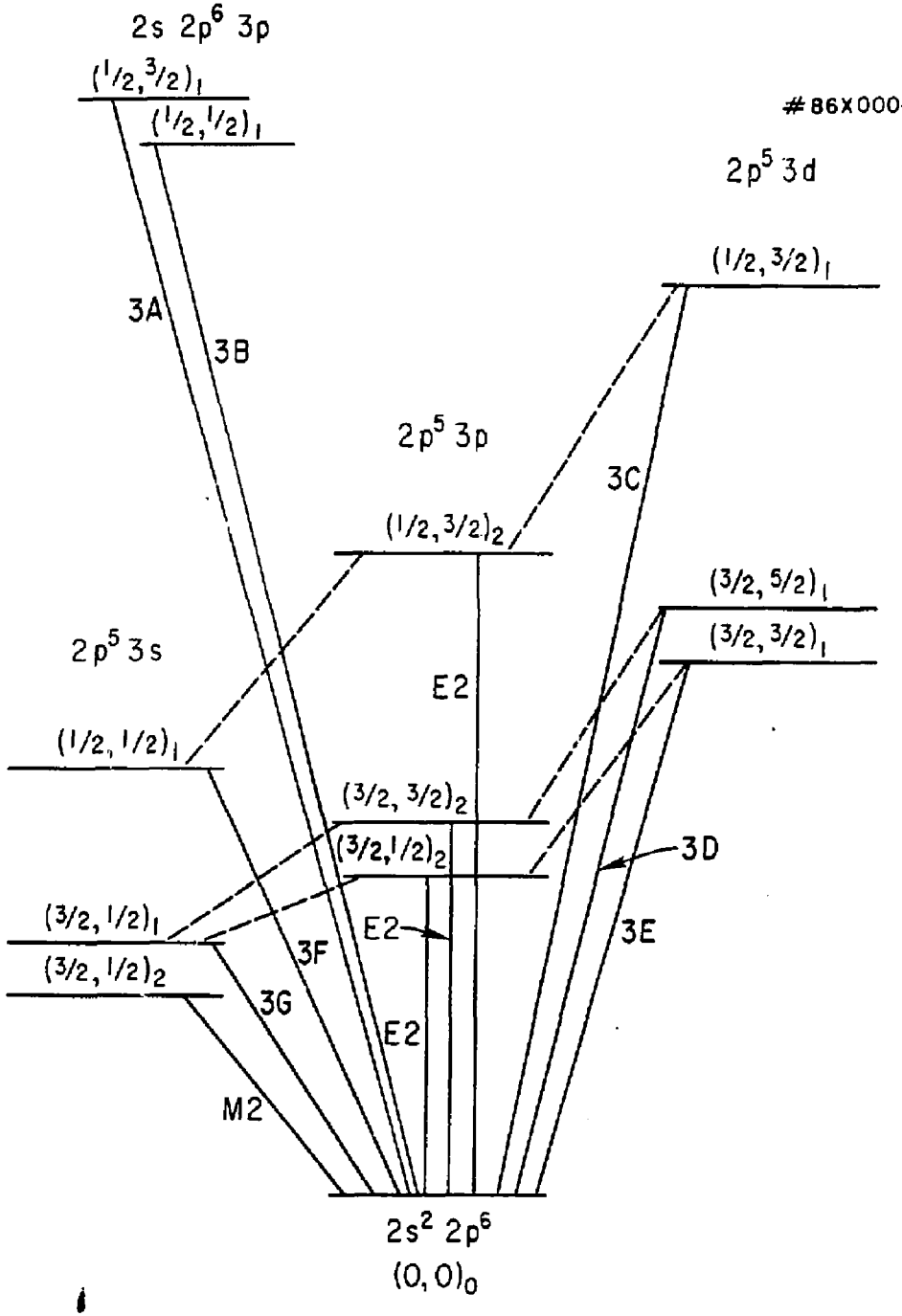
2s 2p⁶ 3p
(1/2, 3/2)₁
(1/2, 1/2)₁
#86X0004
2p⁵ 3d
(1/2, 3/2)₁
3A
3B
2p⁵ 3p
3C
(1/2, 3/2)₂
(3/2, 5/2)₁
(3/2, 3/2)₁
2p⁵ 3s
E2
(1/2, 1/2)₁
(3/2, 3/2)₂
(3/2, 1/2)₂
3D
(3/2, 1/2)₁
E2
3F
3E
(3/2, 1/2)₂
3G
E2
M2
2s² 2p⁶
(0, 0)₀

Fig. 12

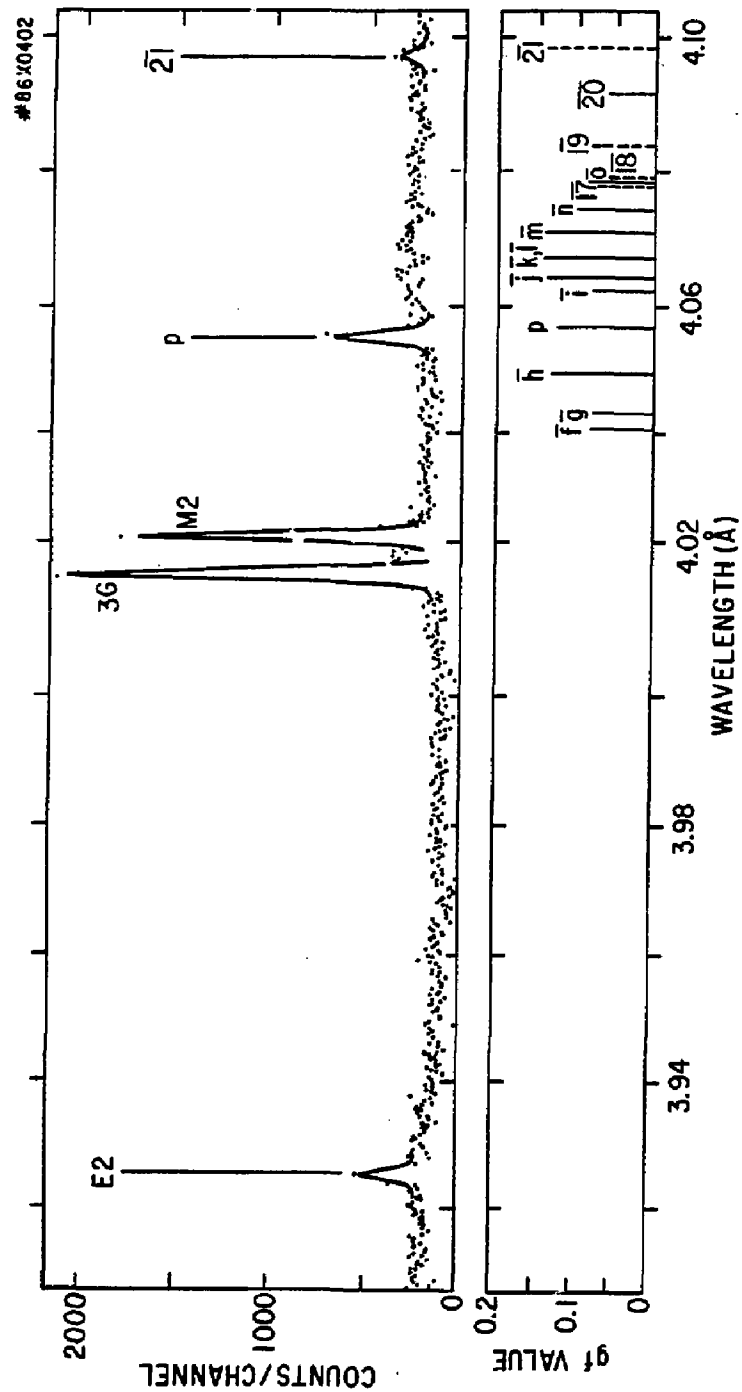
#86X0402
E2
3G
M2
p
$\bar{2}\bar{1}$
2000
1000
0
COUNTS/CHANNEL
0.2
0.1
0
g1 VALUE
3.94
3.98
4.02
4.06
4.10
WAVELENGTH (Å)
$\bar{f}\,\bar{g}$
$\bar{h}$
p
$\bar{i}$
$\bar{j}\,\bar{k}\,\bar{l}\,\bar{m}$
$\bar{n}$
$\bar{1}\bar{7}\,\bar{1}\bar{8}$
$\bar{1}\bar{9}$
$\bar{2}\bar{0}$
$\bar{2}\bar{1}$

Fig. 13

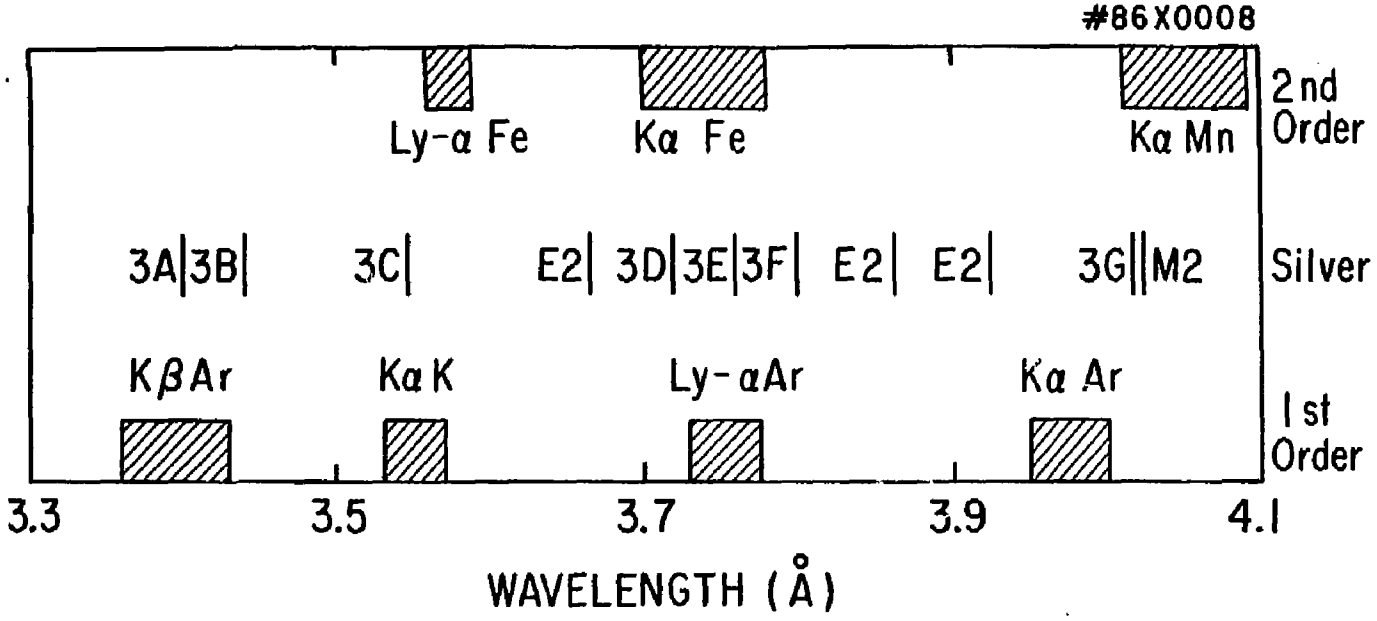
#86X0008
Ly-α Fe
Kα Fe
Kα Mn
2nd Order
3A|3B|
3C|
E2|
3D|3E|3F|
E2|
E2|
3G||M2
Silver
KβAr
KαK
Ly-αAr
Kα Ar
1st Order
3.3
3.5
3.7
3.9
4.1
WAVELENGTH (Å)

Fig. 14

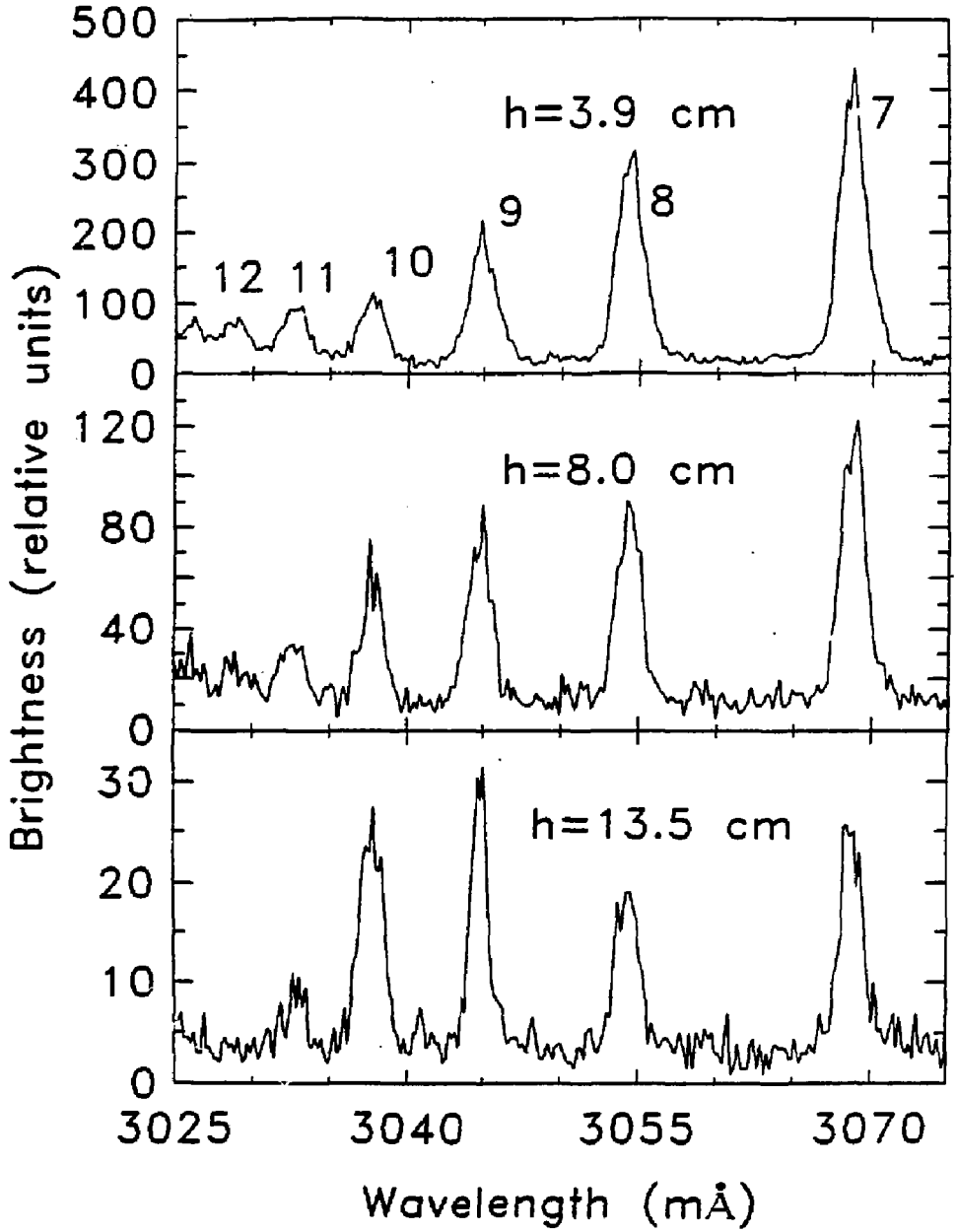
h=3.9 cm
h=8.0 cm
h=13.5 cm
12
11
10
9
8
7
Brightness (relative units)
Wavelength (mÅ)
3025
3040
3055
3070

Fig. 15

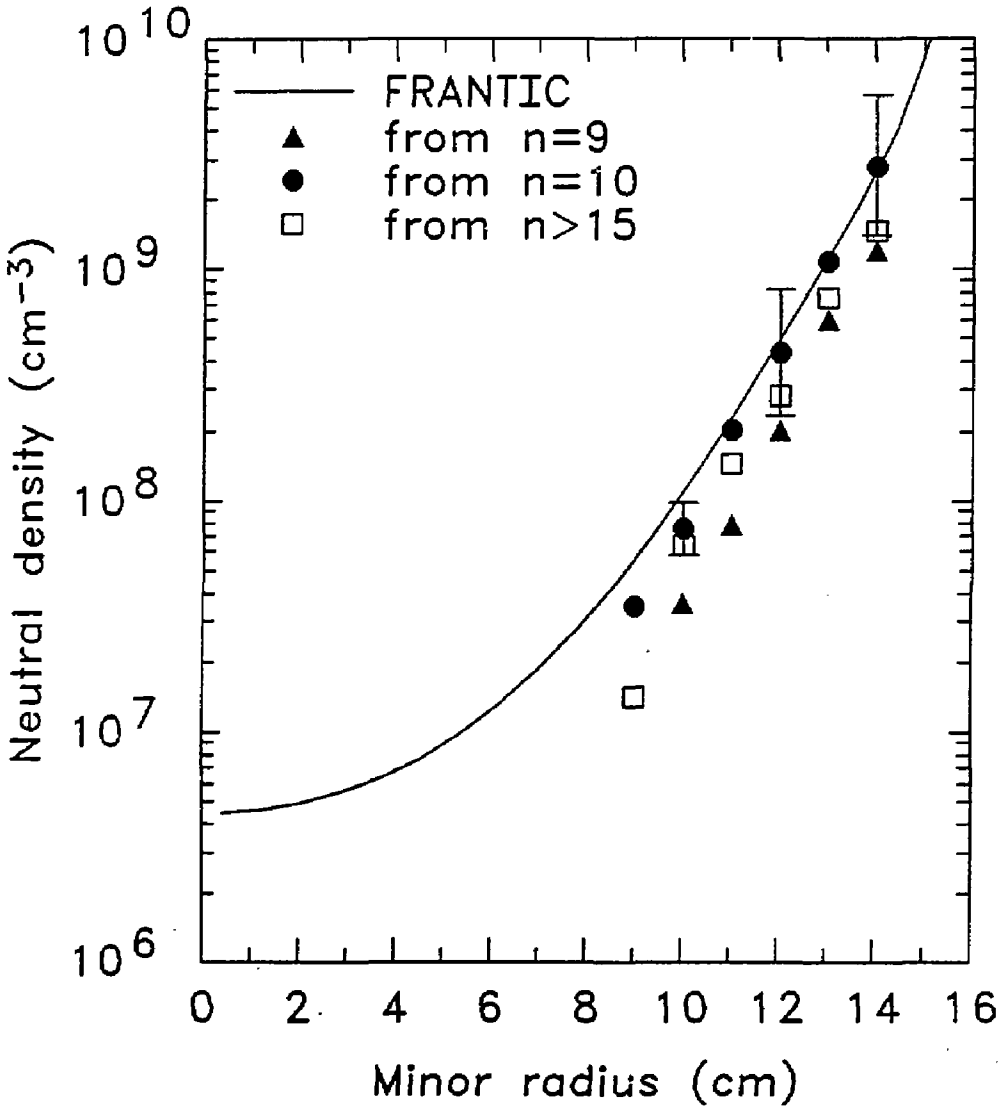
FRANTIC
from n=9
from n=10
from n>15
Neutral density (cm^{-3})
10^{10}
10^{9}
10^{8}
10^{7}
10^{6}
0
2
4
6
8
10
12
14
16
Minor radius (cm)

Fig. 16

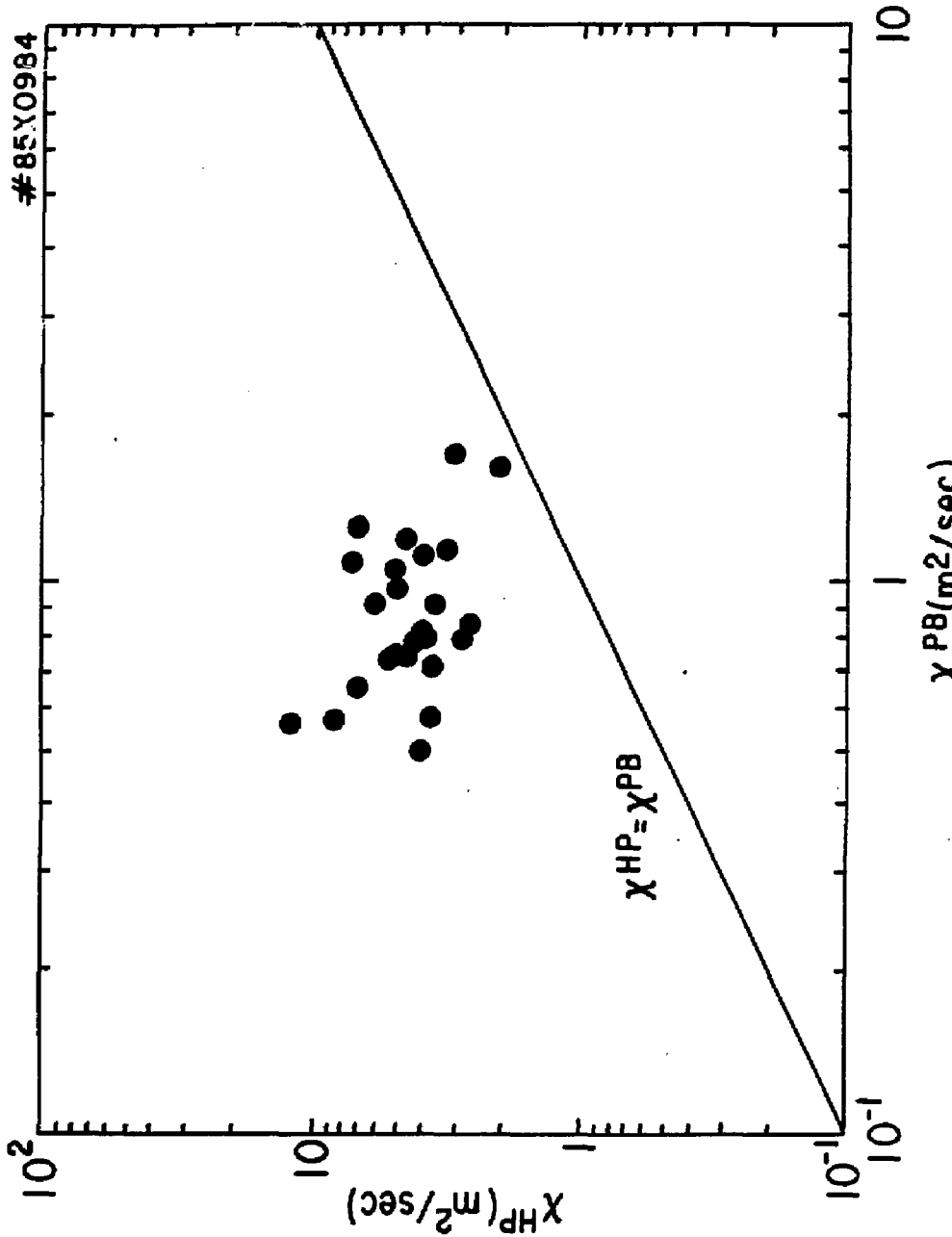
#85X0984
10^2
10
1
10^{-1}
10^{-1}
1
10
$\chi^{HP}(m^2/sec)$
$\chi^{PB}(m^2/sec)$
$\chi^{HP}=\chi^{PB}$

Fig. 17

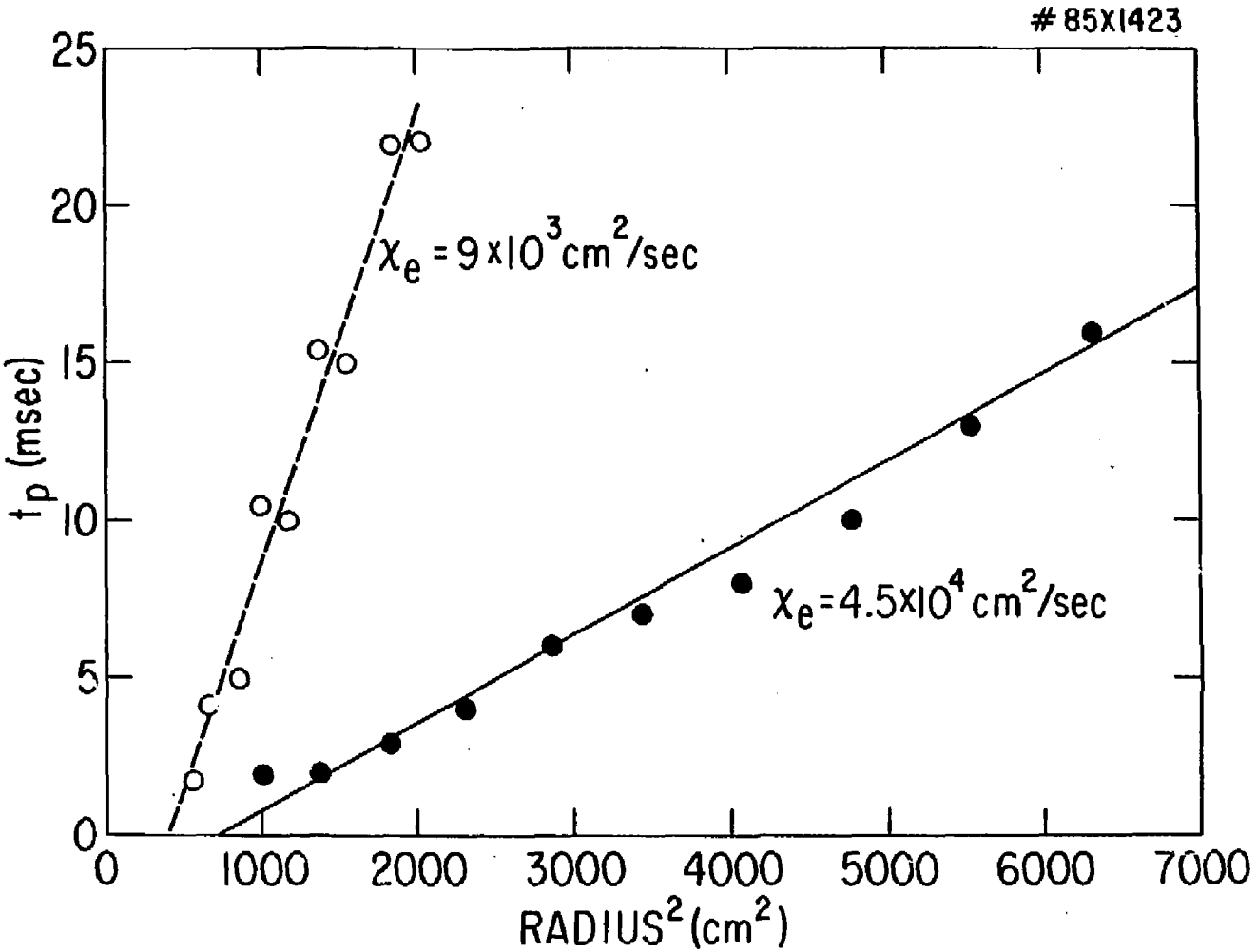
#85X1423
25
20
15
10
5
0
t_p (msec)
$\chi_e = 9 \times 10^3 cm^2/sec$
$\chi_e = 4.5 \times 10^4 cm^2/sec$
0
1000
2000
3000
4000
5000
6000
7000
RADIUS^2(cm^2)

Fig. 18

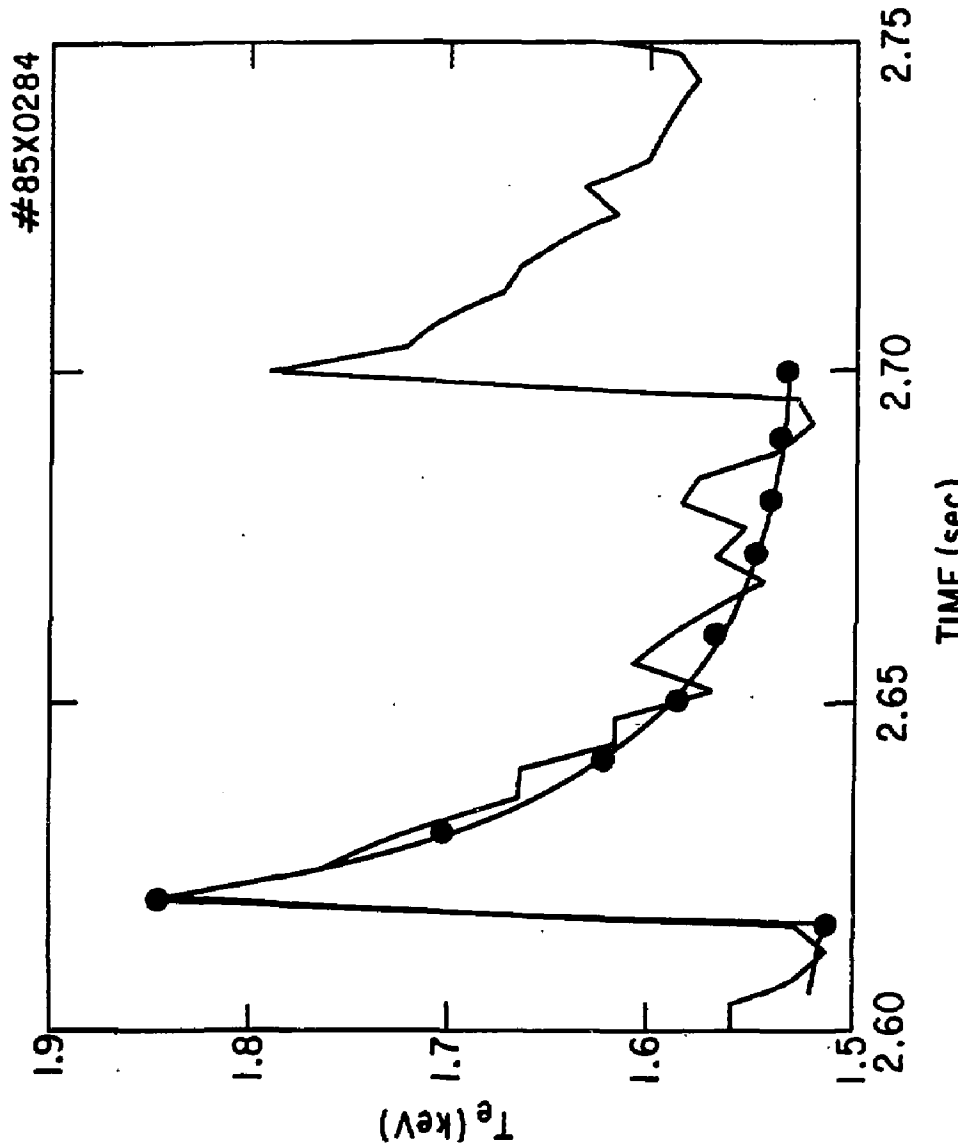

Fig. 19

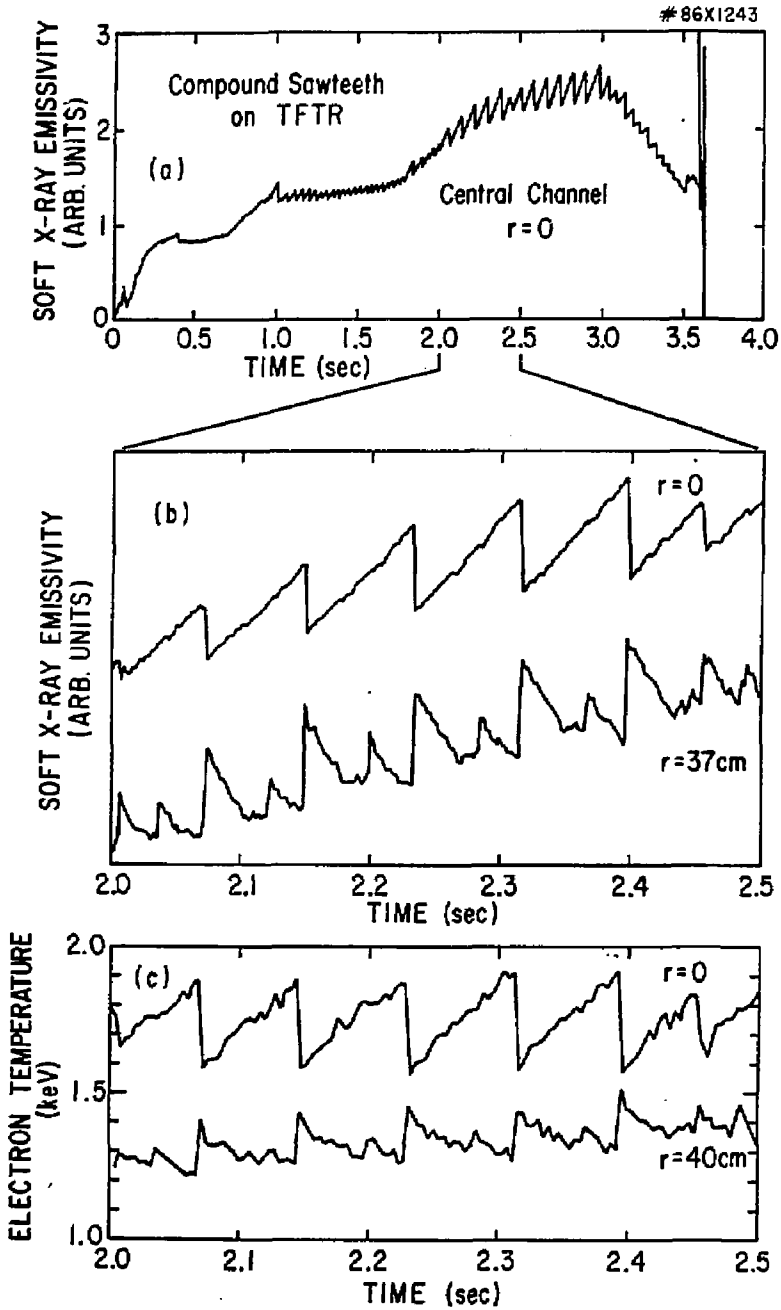
#86X1243
Compound Sawteeth
on TFTR
(a)
Central Channel
r=0
SOFT X-RAY EMISSIVITY
(ARB. UNITS)
TIME (sec)
(b)
r=0
r=37cm
SOFT X-RAY EMISSIVITY
(ARB. UNITS)
TIME (sec)
(c)
r=0
r=40cm
ELECTRON TEMPERATURE
(keV)
TIME (sec)

Fig. 20

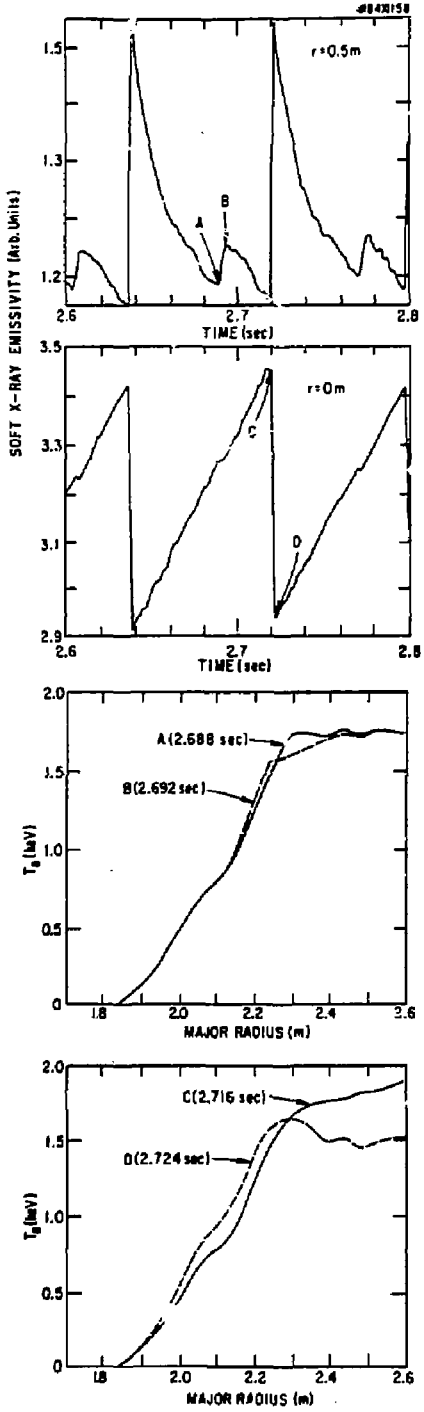
r=0.5m
A
B
SOFT X-RAY EMISSIVITY (Arb. Units)
TIME (sec)
r=0m
C
D
TIME (sec)
A(2.688 sec)
B(2.692 sec)
T_e (keV)
MAJOR RADIUS (m)
C(2.716 sec)
D(2.724 sec)
T_e (keV)
MAJOR RADIUS (m)

Fig. 21

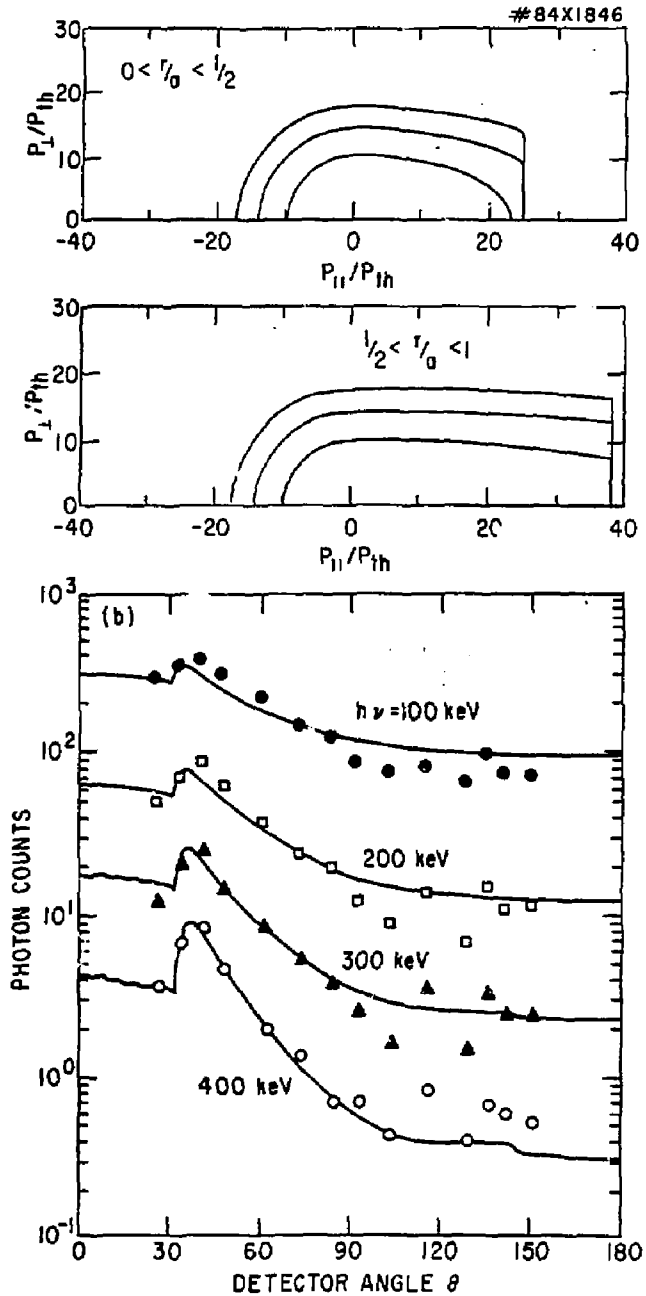
#84X1846
$0 < r/a < 1/2$
$P_\perp/P_{th}$
$P_{||}/P_{th}$
$1/2 < r/a < 1$
(b)
$h\nu$ =100 keV
200 keV
300 keV
400 keV
PHOTON COUNTS
DETECTOR ANGLE θ

Fig. 22

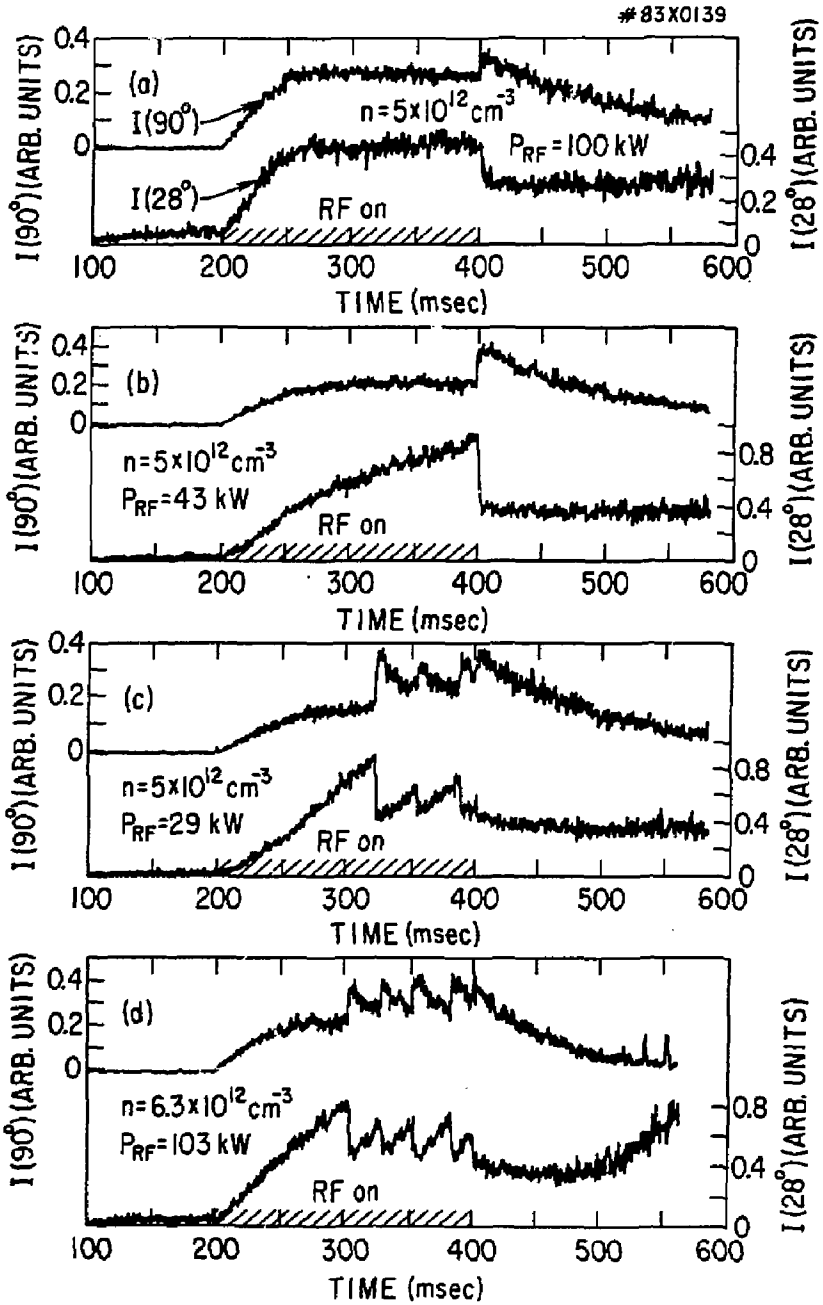
#83X0139
(a)
I(90°)
I(28°)
n=5x10^12 cm^-3
P_RF=100 kW
RF on
(b)
n=5x10^12 cm^-3
P_RF=43 kW
RF on
(c)
n=5x10^12 cm^-3
P_RF=29 kW
RF on
(d)
n=6.3x10^12 cm^-3
P_RF=103 kW
RF on
I(90°)(ARB. UNITS)
I(28°)(ARB. UNITS)
TIME (msec)
100
200
300
400
500
600

Fig. 23

EXTERNAL DISTRIBUTION IN ADDITION TO UC-20

Dr. Frank J. Paoloni, Univ of Wollongong, AUSTRALIA
Prof. M.H. Brennan, Univ Sydney, AUSTRALIA
Plasma Research Lab., Australian Nat. Univ., AUSTRALIA
Prof. I.R. Jones, Flinders Univ., AUSTRALIA
Prof. F. Cap, Inst Theo Phys, AUSTRIA
Prof. M. Heindler, Institut fur Theoretische Physik, AUSTRIA
M. Goossens, Astronomisch Instituut, BELGIUM
Ecole Royale Militaire, Lab de Phys Plasmas, BELGIUM
Com. of European, Dg XII Fusion Prog, BELGIUM
Prof. R. Boucique, Laboratorium voor Natuurkunde, BELGIUM
Dr. P.H. Sakanaka, Univ Estadual, BRAZIL
Instituto De Pesquisas Espaciasi-INPE, BRAZIL
Library, Atomic Energy of Canada Limited, CANADA
Dr. M.P. Bachynski, MPB Technologies, Inc., CANADA
Dr. H.M. Skarsgard, Univ of Saskatchewan, CANADA
Dr. H. Barnard, University of British Columbia, CANADA
Prof. J. Teichmann, Univ. of Montreal, CANADA
Prof. S.R. Sreenivasan, University of Calgary, CANADA
Prof. Tudor W. Johnston, INRS-Energie, CANADA
Dr. C.R. James, Univ. of Alberta, CANADA
Dr. Peter Lukac, Komenskeho Univ, CZECHOSLOVAKIA
The Librarian, Culham Laboratory, ENGLAND
Mrs. S.A. Hutchinson, JET Library, ENGLAND
C. Mouttet, Lab. de Physique des Milieux Ionises, FRANCE
J. Radet, CEN/CADARACHE - Bat 506, FRANCE
Dr. Tom Mual, Academy Bibliographic, HONG KONG
Preprint Library, Cent Res Inst Phys, HUNGARY
Dr. B. Dasgupta, Saha Inst, INDIA
Dr. R.K. Chhajlani, Vikram Univ. INDIA
Dr. P. Kaw, Institute for Plasma Research, INDIA
Dr. Phillip Rosenau, Israel Inst Tech, ISRAEL
Prof. S. Cuperman, Tel Aviv University, ISRAEL
Librarian, Int'l Ctr Theo Phys, ITALY
Prof. G. Rostagni, Univ Di Padova, ITALY
Miss Clelia De Palo, Assoc EURATOM-ENEA, ITALY
Biblioteca, del CNR EURATOM, ITALY
Dr. H. Yamato, Toshiba Res & Dev, JAPAN
Prof. I. Kawakami, Atomic Energy Res. Institute, JAPAN
Prof. Kyoji Nishikawa, Univ of Hiroshima, JAPAN
Direc. Dept. Lg. Tokamak Res. JAERI, JAPAN
Prof. Satoshi Itoh, Kyushu University, JAPAN
Research Info Center, Nagoya University, JAPAN
Prof. S. Tanaka, Kyoto University, JAPAN
Library, Kyoto University, JAPAN
Prof. Nobuyuki Inoue, University of Tokyo, JAPAN
S. Mori, JAERI, JAPAN
M.H. Kim, Korea Advanced Energy Research Institute, KOREA
Prof. D.I. Choi, Adv. Inst Sci & Tech, KOREA
Prof. B.S. Liley, University of Waikato, NEW ZEALAND
Institute of Plasma Physics, PEOPLE'S REPUBLIC OF CHINA
Librarian, Institute of Phys., PEOPLE'S REPUBLIC OF CHINA
Library, Tsing Hua University, PEOPLE'S REPUBLIC OF CHINA
Z. Li, Southwest Inst. Physics, PEOPLE'S REPUBLIC OF CHINA
Prof. J.A.C. Cabral, Inst Superior Tecn, PORTUGAL
Dr. Octavian Petrus, AL I CUZA University, ROMANIA
Dr. Johan de Villiers, Plasma Physics, AEC, SO AFRICA
Prof. M.A. Hellberg, University of Natal, SO AFRICA
Fusion Div. Library, JEN, SPAIN
Dr. Lennart Stenflo, University of UMEA, SWEDEN
Library, Royal Inst Tech, SWEDEN
Prof. Hans Wilhelmson, Chalmers Univ Tech, SWEDEN
Centre Phys des Plasmas, Ecole Polytech Fed, SWITZERLAND
Bibliotheek, Fom-Inst Voor Plasma-Fysica, THE NETHERLANDS
Dr. O.D. Ryutov, Siberian Acad Sci, USSR
Dr. G.A. Eliseev, Kurchatov Institute, USSR
Dr. V.A. Glukhikh, Inst Electro-Physical, USSR
Dr. V.T. Tolok, Inst. Phys. Tech. USSR
Dr. L.M. Kovrizhnykh, Institute Gen. Physics, USSR
Prof. T.J.M. Boyd, Univ College N Wales, WALES
Nuclear Res. Establishment, Julich Ltd., W. GERMANY
Bibliothek, Inst. Fur Plasmaforschung, W. GERMANY
Dr. K. Schindler, Ruhr Universitat, W. GERMANY
ASDEX Reading Rm, IPP/Max-Planck-Institut fur Plasmaphysik, W. GERMANY
Librarian, Max-Planck Institut, W. GERMANY
Prof. R.K. Janev, Inst Phys, YUGOSLAVIA